

Original Article

Cite this article: Langone A, Simonetti M, Corvò S, Bonazzi M, Maino M, Orlando A, Braschi E, and Piazzolo S. Reactive and resilient: the contrasting behaviour of monazite and titanite during deformation (the Forno-Rosarolo shear zone; Ivrea-Verbano Zone). *Geological Magazine* 162(e18): 1–24. <https://doi.org/10.1017/S0016756825100022>

Received: 29 July 2024

Revised: 7 March 2025

Accepted: 2 May 2025

Keywords:


Mylonites; monazite; titanite; petrochronology; geochemistry; microstructure; U–(Th–)Pb

Corresponding authors: Antonio Langone;

Email: antonio.langone@unipv.it,

Stefania Corvò; Email: stefania.corvo@unipv.it

Reactive and resilient: the contrasting behaviour of monazite and titanite during deformation (the Forno-Rosarolo shear zone; Ivrea-Verbano Zone)

Antonio Langone¹ , Matteo Simonetti², Stefania Corvò^{1,3}, Mattia Bonazzi^{1,3}, Matteo Maino^{1,3}, Andrea Orlando⁴, Eleonora Braschi⁴ and Sandra Piazzolo⁵

¹Department of Earth and Environmental Sciences, University of Pavia, Pavia, Italy; ²Geological Survey of Italy, ISPRA, Roma, Italy; ³Institute of Geosciences and Earth Resources of Pavia, C.N.R., Pavia, Italy; ⁴Institute of Geosciences and Earth Resources of Florence, C.N.R., Firenze, Italy and ⁵School of Earth and Environment, University of Leeds, Leeds, UK

Abstract

Dating the shear zone activity remains challenging and depends on geochronometer reactivity. We investigate the Forno-Rosarolo Shear Zone (Ivrea-Verbano Zone, Italy), developed in the intermediate-low continental crust under amphibolite-facies conditions. Sheared paragneisses and calc-silicates were dated using in situ U–(Th–)Pb monazite and titanite geochronology. Three monazite generations (MNZI–III) were identified based on microstructural position, internal features, chemical zoning (Th, Y) and isotopic data. Deformation was mainly recorded by MNZII, with high-Y domains yielding Triassic dates (average ages of: 238 ± 8 and 222 ± 8 Ma). Rare, highly fractured or porous MNZIII grains provided younger dates (202 ± 8 to 184 ± 6 Ma). MNZI, abundant in protomylonites, retains regional metamorphism, linking monazite U–Th–Pb data to fabric evolution. Titanite shows different zoning features and chemistry as a function of the surrounding mineral assemblage: (i) strongly zoned grains are mostly associated with silicate-rich layers; (ii) homogeneous grains are generally within the silicate-poor layers. Both types show a decoupling between chemistry, almost completely related to the peak metamorphism, and U–Pb isotopes. Deformation microstructures promoted a total reset of the U–Pb dataset at the beginning of deformation and a subsequent volume diffusion through the grains: the innermost domains of both titanite types provide a Triassic lower intercept age (240 ± 5 Ma) while the rims/tips, locally coinciding with high strained portions, define an alignment of isotopic data with a Jurassic lower intercept age (186 ± 6 Ma). This study highlights how combining monazite and titanite geochronology refines the timing and duration of deformation, particularly in large-scale shear zones involving different lithologies.

1. Introduction

Constraining the timing of ductile deformation is crucial for understanding the tectono-metamorphic evolution of intermediate-lower crustal domains in both continental and oceanic crust (e.g. Xypolias, 2010; Oriolo *et al.* 2018). Mylonites reflect zones of high strain where dominantly ductile deformation has been localized. Mylonitic shear zones occur at all scales in the lithosphere and may provide pathways that localize fluids and secondary alteration (e.g. Beach, 1976; Austrheim, 2013; Kirkland *et al.* 2023). These rocks may thus preserve key evidence for the kinematics and structure of an orogen as well as of rift-related systems. Dating the evolution of the shear zones has been described as one of the most difficult problems in geochronology (e.g. Oriolo *et al.* 2018; Kirkland *et al.* 2023). In addition to the dating of major fabric-forming minerals, in situ geochronology or petrochronology on minor and accessory minerals may provide direct constraints on the timing of deformation (e.g. Piazzolo *et al.* 2012) as it allows linking isotopic dating, microstructures, geochemistry and thermobarometry. In recent years, the combination, simultaneously or not, of isotopic ratios and trace element for accessory and minor minerals with in situ techniques, opens the possibility to date the small syn-kinematic domains developed on pre-existing grains (e.g. Simonetti *et al.* 2020, 2021b; Carosi *et al.* 2022; Moser *et al.* 2022; Walters *et al.* 2022; Kirkland *et al.* 2023; Kavanagh-Lepage *et al.* 2023; Corvò *et al.* 2023). Among the accessory minerals, monazite and titanite are the most promising being present in different rock types and, most important being more reactive with respect to other accessory minerals, i.e. zircon. Both chronometers have been shown to develop chemical zoning as function of metamorphic reactions with and without deformation allowing to link the ages to specific geologic events (Engi, 2017; Hetherington *et al.* 2017; Kohn, 2017; Kohn *et al.* 2017).

© The Author(s), 2025. Published by Cambridge University Press. This is an Open Access article, distributed under the terms of the Creative Commons Attribution licence (<https://creativecommons.org/licenses/by/4.0/>), which permits unrestricted re-use, distribution and reproduction, provided the original article is properly cited.



The usefulness of monazite as a geochronometer is due to its lattice properties allowing it to contain high concentration of Th and U and low amounts of common-Pb (Parrish, 1990). Monazite is common in metapelitic/metapsammitic rocks with Ca-poor and Al-rich bulk compositions at metamorphic conditions above upper greenschist facies (e.g. Spear & Pyle, 2010). Unlike zircon, monazite has a higher reactivity, it is able to preserve isotopic inheritance and to record P-T conditions from prograde to retrograde (e.g. Langone *et al.* 2011). Monazite may develop chemical zoning that can be linked to a specific metamorphic reaction related to static or dynamic (re)crystallization of both major and accessory rock-forming minerals (e.g. Wawrzenitz *et al.* 2012; Hetherington *et al.* 2017). In the last years, the combination of in situ U–Th–Pb data with the geochemical composition of the dated monazites allowed to establish the timing of complex geologic events (e.g. Shaw *et al.* 2001; Williams & Jercinovic, 2002; Rasmussen & Muhling, 2007; Di Vincenzo *et al.* 2007; Janots *et al.* 2012; Wawrzenitz *et al.* 2012; Williams & Jercinovic, 2012; Didier *et al.* 2014; Grand'Homme *et al.* 2016; Kohn, 2016; Regis *et al.* 2016; Bosse & Villa, 2019; Bergemann *et al.* 2020; Simonetti *et al.* 2020, 2021b; Schulz, 2021; Carosi *et al.* 2022). Although monazite can be useful to date tectonic events in rocks from the middle and lower crust (Erickson *et al.* 2015; Williams & Jercinovic, 2012; Mottram & Cottle, 2024), it has been documented that monazite is able to record shearing by fluid-assisted dissolution and growth on rims at low amphibolite-facies metamorphic condition (e.g. Terry *et al.* 2000) or even lower metamorphic conditions (e.g. Shaw *et al.* 2001).

Recently, it has been demonstrated that titanite microstructures can be used to date hypervelocity meteorite impacts (e.g. Papapavlou *et al.* 2017; McGregor *et al.* 2021) as well as the activity of ductile shear zones developed within continental crustal rocks (e.g. Gordon *et al.* 2021; Moser *et al.* 2022; Kavanagh-Lepage *et al.* 2023; Corvò *et al.* 2023). Conversely to monazite, the adoption of titanite as a geochronometer is complicated by two main issues. Firstly, it has a strong affinity for Pb and thus it may incorporate common lead during crystallization (e.g. Kohn, 2017). Consequently, most titanite U–Pb measurements require correction for substantial common Pb before age interpretations, e.g. by regressing less radiogenic and more radiogenic measurements on inverse isochrons (Tera-Wasserburg diagrams) to derive an age. Secondly, the temperature range for diffusive Pb-loss within the grains is somewhat disputed. Titanite has been traditionally considered as a thermochronometer with closure temperatures of 650°C and 750°C determined experimentally for titanite crystals with 0.5 and 5mm radii, respectively, and considering a cooling of about 5°C/Myr (Cherniak, 1993). In contrast with the experimental works, several studies on natural titanite grains suggest that the U–Pb isotope system may be resistant to volume diffusion at temperature of up to 800°C (Kohn, 2017; Hartnady *et al.* 2019) providing crystallization ages (and not cooling ages) and referring to titanite as a petrochronometer (e.g. Hartnady *et al.* 2019; Holder *et al.* 2019; Olierook *et al.* 2019; Scibiowski *et al.* 2019; Kirkland *et al.* 2020; Gordon *et al.* 2021; Moser *et al.* 2022; Walters *et al.* 2022). Besides these two main issues, several authors (e.g. Gordon *et al.* 2021; Moser *et al.* 2022; Kavanagh-Lepage *et al.* 2023; Corvò *et al.* 2023) highlighted a decoupling between the U–Pb isotopic system and some trace elements and a strong dependence on the mineral assemblage of the hosting microdomain for titanite during deformation (e.g. Corvò *et al.* 2023).

In this contribution, we aim to assess the robustness and utility of the two geochronometers in deciphering the tectono-

metamorphic history of high-strain rocks. We present monazite and titanite microstructural, chemical and isotopic data from mylonitic paragneisses and calc-silicates from an extensional shear zone affecting the continental crustal section of the Ivrea-Verbano Zone. This zone is ideally suited for our study since it has been the object of detail reconstructions of strain distribution and lithological make-up. It has been shown that both monazite and titanite are present in the main lithologies. Importantly, the zone records different tectono-metamorphic events, the timing of which remains disputed (e.g. Siegesmund *et al.* 2008; Garde *et al.* 2015; Simonetti *et al.* 2023). Here, we (i) describe the behaviour of monazite and titanite under the same shearing conditions, (ii) shed light on the timing of deformation by U–Th–Pb dating of monazite and titanite and on the petrologic evolution of mylonites during deformation and (iii) discuss the complementary and contrasting utility of these two geochronometers in dating deformation in mid- to lower-crustal rocks.

2. Geological setting

The Ivrea-Verbano Zone (IVZ) in north-western Italy represents a cross-section through the middle to lower continental crust of the Southern Alpine basement (Figure 1a). During the Alpine collision, the IVZ underwent vertical exhumation and open folding, but it escaped the metamorphic overprint (Henk *et al.* 1997; Rutter *et al.* 2007; Wolff *et al.* 2012). The IVZ is delimited by the Insubric Line northward, while south-eastward, it is juxtaposed to the Serie dei Laghi Unit by the Late-Variscan Cossato–Mergozzo–Brissago Line, which is in turn crosscut by the Pogallo Line (Figure 1a; Boriani *et al.* 1990).

The IVZ is traditionally subdivided into three main units (Figure 1a), from NW-SE: (i) the mantle peridotites; (ii) the Mafic Complex and (iii) a volcano-sedimentary metamorphic sequence, namely the Kinzigite Formation. The latter is considered as the original upper part of the tilted crustal section made up of a heterogeneous group of metasediments, comprising mainly metapelites with intercalated metabasic rocks (i.e. volcanic sediments and MORB-like lavas) and minor marbles/calc-silicates and quartzites (Zingg, 1990; Schmid, 1993; Quick *et al.* 2002; Kunz *et al.* 2014). At a regional scale, peak metamorphic grade decreases from granulite (~900°C and 900 MPa) to amphibolite facies (~600°C and ~400 MPa) from NW to SE (Schmid & Wood, 1976; Brodie & Rutter, 1987; Zingg, 1990; Schmid, 1993; Redler *et al.* 2012; Kunz *et al.* 2014; Kunz & White, 2019). The highest degree of metamorphic conditions has been recorded by paragneiss septa (i.e. depleted granulite) forming layers within the Mafic Complex (Figure 1a; Sinigoi *et al.* 1996; Ewing *et al.* 2013). The progressive switch at the mid- to lower crustal levels from granulite to amphibolite facies is marked by a transition zone of ~1–5 kilometres (Figure 1b) that experienced extensive migmatization processes (e.g. Redler *et al.* 2012; Kunz *et al.* 2014; Carvalho *et al.* 2019). In the north-eastern part of the IVZ, this transition zone hosts two mylonitic shear zones, namely the Anzola (Brodie & Rutter, 1987; Corvò *et al.* 2022, 2023) and the Forno-Rosarolo shear zones (Siegesmund *et al.* 2008; Simonetti *et al.* 2023). Although described as separate shear zones and often named in different ways (see Simonetti *et al.* 2021a), these structures have been interpreted as a single fault system, with NNE-SSW strike (e.g. Rutter *et al.* 2007), associated to the Triassic-Jurassic (180–230 Ma) rift-related tectonic (Beltrando *et al.* 2015; Petri *et al.* 2019; Simonetti *et al.* 2023; Corvò *et al.* 2023). In this time interval, crustal thinning (<10 km thick) was accommodated by several

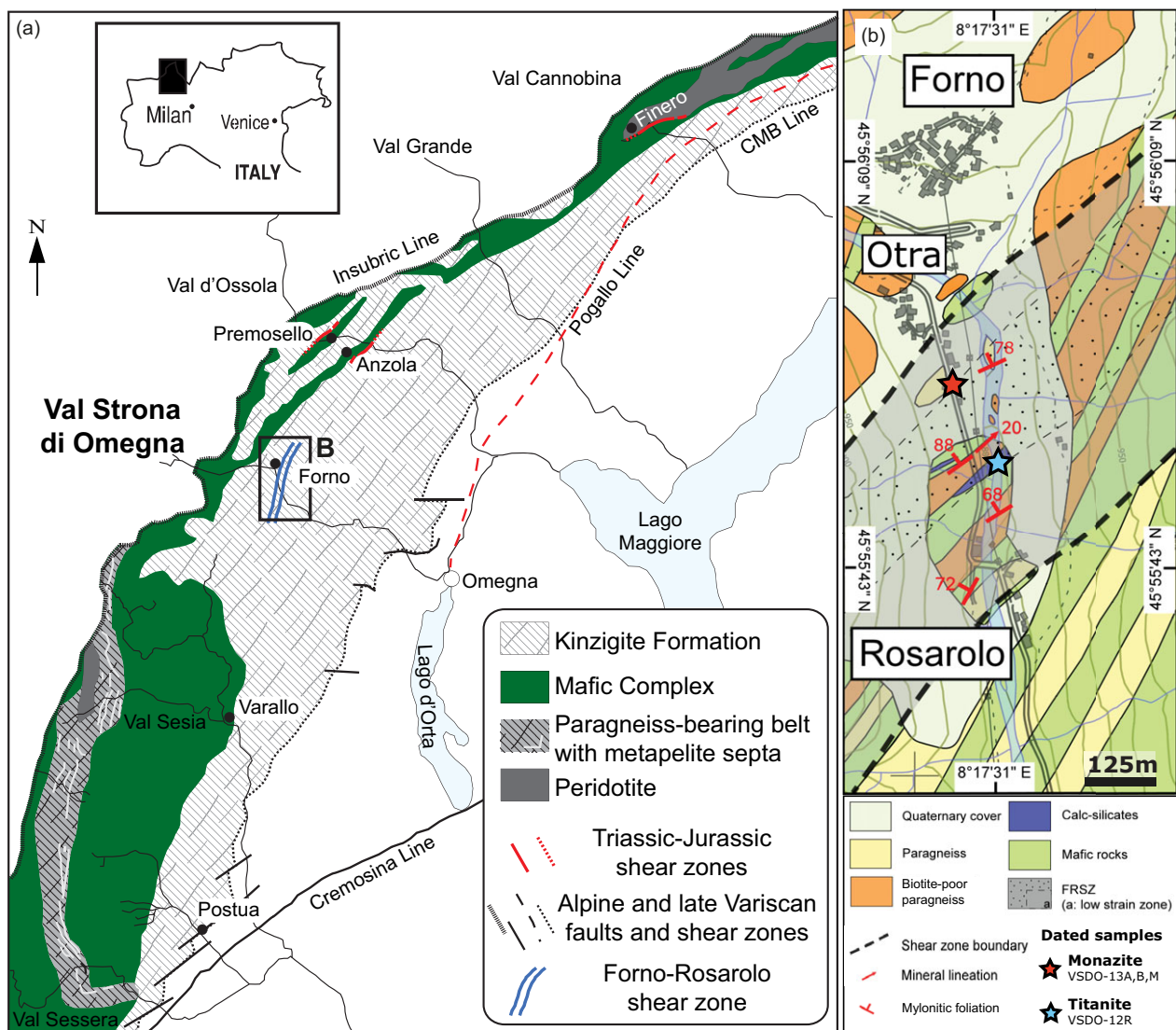


Figure 1. Geological sketch map of the Ivrea-Verbano Zone, modified after Ewing *et al.* (2015), Simonetti *et al.* (2021a, 2023) and Corvò *et al.* (2022). In (a) the locations of Triassic-Jurassic shear zones (in red) dated by the U-Pb method are after Langone *et al.* 2018 (Finero area), Corvò *et al.* 2023 (Anzola area) and Corvò *et al.*, 2025 (Premosello area). The studied area is delimited by the black box. (b) Schematic structural and geological map of the Forno-Rosarolo shear zone (modified after Bertolani, 1968 and Simonetti *et al.* 2023) with the location of samples analysed for the geochronology.

shear zones active during different phases of rifting (Manatschal *et al.* 2007; Mohn *et al.* 2012) at different crustal levels (e.g. Beltrando *et al.* 2015).

2.a. Geochronological background

Several authors, by using geochronological and/or thermochronological techniques, aimed to constrain the timing of the main geodynamic episodes that characterized the evolution of the crustal section of the IVZ. Here, we report a summary of the main tectono-metamorphic event well recorded by both geo- and thermochronometers.

The rare occurrence of Carboniferous (Pennsylvanian) metamorphic (i.e. 316 ± 3 Ma U-Pb on zircon, Ewing *et al.* 2013, 2015; 311 ± 2 Ma garnet-whole rock Lu-Hf isochrons, Connop *et al.* 2024) and magmatic ages (i.e. 314 ± 5 Ma U-Pb on zircon Klötzli *et al.* 2014) indicates that the pervasive amphibolite- and granulite-

facies mineral parageneses of the IVZ formed after the peak of Variscan compressional deformation and plutonism.

The IVZ recorded mostly tectono-metamorphic and magmatic events during the Permian as documented by dating of different accessory minerals from metamorphic (e.g. Henk *et al.* 1997; Vavra *et al.* 1999; Guergouz *et al.* 2018; Kunz *et al.* 2018; Williams *et al.* 2022; Wyatt *et al.* 2022; Corvò *et al.* 2024) and magmatic rocks (e.g. Peressini *et al.* 2007; Karakas *et al.* 2019). This High-Temperature (HT) event has been confirmed also recently by both in situ garnet U-Pb dating (Bartoli *et al.* 2024) and garnet-whole rock Lu-Hf isochrons (Connop *et al.* 2024) of metamorphic samples across the crustal section. The pervasive amphibolite- and granulite-facies mineral parageneses formed during the Permian lithospheric thinning, well documented across the Alps (e.g. Schuster & Stüwe, 2008).

The geochronological studies performed on metamorphic rocks across the IVZ crustal section revealed also that the HT conditions

Table 1. Summary of mineral assemblage, accessory minerals, type of fabric and analysed minerals for the studied samples

Sample name (coordinates)	Rock type	Mineral assemblage (accessory minerals)	Type of fabric	Analysed accessory mineral for geochronology
VSDO-13B (45.932198, 8.290887)	biotite-poor paragneiss	Sil, Grt, Qz, Pl, Kfs, Bt (Mnz, Rt, Zrn)	protomylonitic fabric	monazite
VSDO-13A (45.932198, 8.290887)	biotite-rich paragneisses	Bt, Sil, Grt, Qz, Pl, Kfs (Mnz, Rt, Zrn)	protomylonitic fabric	monazite
VSDO-13M1; VSDO-13M2; VSDO-13M4; (45.932412, 8.292021)	biotite-rich paragneisses	Bt, Sil, Grt, Qz, Pl, Kfs (Mnz, Rt, Zrn)	mylonitic (locally ultramylonitic) fabric	monazite
VSDO-12R2B (45.930638, 8.292250)	calc-silicate	Cal, Pl, Kfs, Amp, Cpx, Bt, Bt ± Grt, Scp, Aln (Ttn, Zrn, Ap)	mylonitic fabric	titanite

persisted for several Myr. Thanks to a systematic study of textures, REE content and U–Pb ages of zircon and monazite grains, Guergouz *et al.* (2018) inferred that the minimum duration for high-temperature metamorphism should be between 20 and 30 Myr. Kunz *et al.* (2018) dated granulitic rocks by zircon U–Pb and suggested that the HT metamorphic conditions lasted for a longer time interval, up to 60 Myr. A recent study of monazite across the crustal section exposed in the Valle Strona di Omegna reported dates mostly in the range 240–320 Ma with two main peaks at circa 290 and 270 Ma (Williams *et al.* 2022). According to these authors, the monazite textural and chemical features indicate that these dates record the timing of pre-peak to peak metamorphic conditions. The long-lasting persistency of HT conditions agrees with the model proposed by Schuster & Stüwe (2021) suggesting lithospheric thinning with negligible surface subsidence between 290 and 240 Ma.

Magmatism and deformation associated with the Triassic–Jurassic Tethyan rifting largely overprinted the Permian crustal section (e.g. Beltrando *et al.* 2015). A review of both geochronological and thermochronological Triassic–Jurassic data has been recently published (Simonetti *et al.* 2021a). Here, we summarize isotopic data related to post-Permian deformation events recorded by the IVZ crustal section. One of the oldest studies focused on deformation was provided by Brodie *et al.* (1989) by dating with Ar–Ar method syn-kinematic hornblende from mylonitic amphibolites of the Anzola shear zone (Figure 1a). These authors obtained two ages at 215±5 Ma and 210±5 Ma that were interpreted by the authors in terms of the effects of grain-size reduction on the closure temperature for argon in hornblende and helped further to chart the cooling history of the rocks. The activity of the Anzola Shear Zone has been recently constrained by Corvò *et al.* (2023) by U–Pb petrochronology of titanite from mylonites consisting of alternating amphibolites and calc-silicates. These authors obtained a Jurassic lower intercept age (188±2 Ma) from rims/tips of titanite grains showing different chemistry and a major concentration of dislocations with respect to the inner domains. The Jurassic deformation was also recorded at different crustal levels by rocks showing different metamorphic conditions. The most prominent rifting-related structure in the southern portion of the IVZ is the Pogallo Line, which is interpreted as a low-angle normal fault that accommodated thinning (Hodges & Fountain, 1984) between Triassic and Jurassic age (ca. 210 and 170 Ma; Zingg, 1990; Mulch *et al.* 2002; Wolff *et al.* 2012) under decreasing temperatures from amphibolite- to greenschist-facies conditions. In the northern sector of the IVZ, Late Triassic to Early Jurassic ductile shear zones developed within (ultra)mafic rocks of the lower crust (U–Pb

zircon data, Langone *et al.* 2018; hornblende Ar–Ar data, Boriani & Villa, 1997 of mylonitic metagabbro in Val Cannobina) and mantle peridotites (e.g. U–Pb zircon data, Corvò *et al.* 2020) under upper-amphibolite to granulite-facies conditions (Brodie, 1981; Kenkmann, 2000; Kenkmann & Dresen, 2002; Degli Alessandrini, 2018; Langone *et al.* 2018).

3. Methods

3.a. Sampling strategy

For geochronology, we selected metapelites showing different microstructural features (protomylonitic and mylonitic fabric) and composition (biotite-rich and biotite-poor) for monazite dating and a calc-silicate sample for titanite dating (Table 1). All the samples are coming from the transition between the high-strain and the low-strain zones of the shear zone (Simonetti *et al.* 2023). Monazite samples were collected from one outcrop along the road whereas titanite-bearing samples are coming from another outcrop along the river, about 150m southward (Figure 1b). Monazite was analysed within six thin-sections from a biotite-poor (VSDO-13B) and two biotite-rich paragneisses (VSDO-13A and VSDO-13M; Figure 2; Table 1).

Titanite was studied on different thin-sections of mylonitic calc-silicates. The samples were cut parallel to the mineral lineation and perpendicular to the main foliation, therefore, along the XZ plane of the finite strain ellipsoid. The analyses were carried out in a (50 µm-thick) thin-section of a representative sample (VSDO-12R2B; Table 1; Figure 3).

3.b. Monazite and titanite chemistry

Thin-sections were polished, C-coated and inspected using a Scanning Electron Microscope (SEM; Mira3, TESCAN) hosted at the Earth and Environmental Sciences Department of Pavia University, in order to observe monazite and titanite microstructural position, internal features and zoning in back-scattered electron (BSE).

The composition and zoning of monazite grains were characterized by acquiring X-ray maps (for P, Ca, Y, La, Ce, Pr, Nd, Sm, Eu, Gd, Th and U) and chemical analyses with a JEOL 8200 Super Probe electron microprobe hosted at the University of Milano (Italy) and a CAMECA SX-Five microprobe hosted in the Service CAMPARIS Sorbonne University (Paris). An accelerating voltage of 15 kV, a beam current of 5 and of 150 nA (respectively for chemical analysis and X-ray maps) and a spot size of 1 µm were used for the JEOL 8200 Super Probe. The CAMECA SX-Five

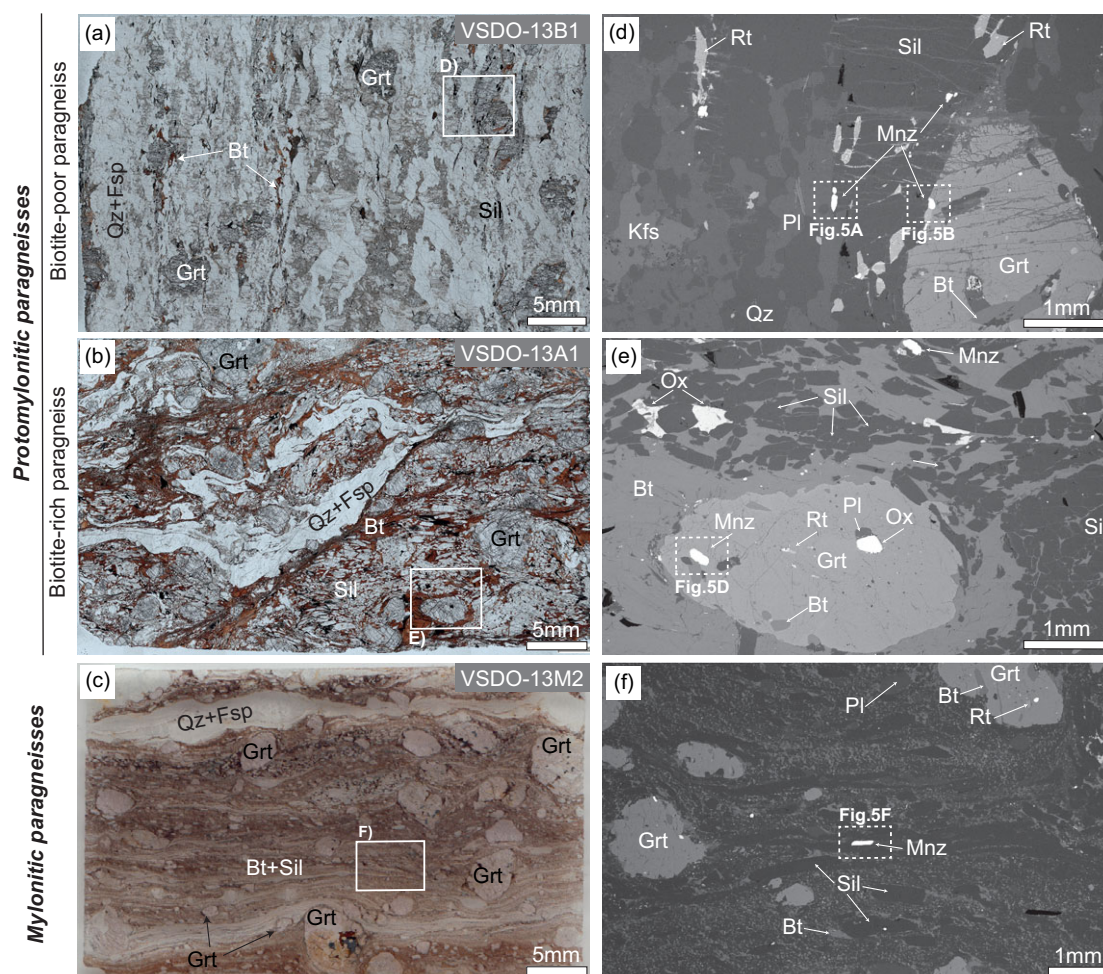


Figure 2. Thin-section scans (a–c) of sheared paragneisses and BSE images (d–f) showing some textural and petrographic details. Dashed white boxes on BSE images in d–f, enclose some monazite grains whose internal zoning is shown in Figure 5. Mineral abbreviations after Whitney & Evans (2010).

microprobe was set at 15 kV, a beam current of 5 and of 230 nA for the maps. Monazite formula, normalized to 16 oxygens, was obtained with an in-house Excel spreadsheet. Results are provided in Table S1 (Supplementary Material).

X-ray compositional maps (Si, Ti, Al, Ca, Fe, F, Zr, Nb, La, Ce and Nd) and chemical analyses (Si, Ti, Al, Fe, Mn, Ca, Na, P, Zr, Nb, La, Ce, Nd, Cl and F) of titanite were acquired with a JEOL 8230 Super Probe electron microprobe hosted at the University of Florence (Italy). An accelerating voltage of 15 kV, a beam current of 20 and of 100 nA (respectively for chemical analysis and X-ray maps) and a spot size of 1 μm were used for chemical analyses, whereas variable spot size was considered according to map size for the compositional map. Titanite stoichiometry was calculated using the method of Oberti *et al.* (1981). Results are provided in Table S2 (Supplementary Material).

3.c. Imaging and quantitative microstructural analysis (EBSD)

In order to analyse the microstructural features, several monazite and titanite grains from the studied samples were selected for obtaining Electron-Backscattered Diffraction (EBSD) maps in thin-section using the FEI Quanta 650 FEG-ESEM (with Oxford X-max 80 SDD EDS, Oxford/HKL Nordleys EBSD system and Aztec software) at the LEMAS, University of Leeds, UK. A working

distance of 20 mm, a 70° stage tilt, accelerating voltage of 20 kV and a step size of 0.5–1 μm were used for analyses. Post processing included correcting for wild spikes and down to a 5 nearest neighbour zero solutions correction. Quantitative orientation analyses are presented by maps, pole and dislocation analysis methods using AztecCrystal 2.2 (Oxford Instruments). Pole figures (PF) for monazite and titanite crystallographic system (monoclinic; (100), (010), (001), lower hemisphere projection on plane XZ), and misorientation profiles tendentially from core to rim or from the low to high distorted domains across the grains are used to assess orientation changes locally and within whole grains.

So-called Grain Reference Orientation Deviation (GROD) maps are presented to highlight the pattern and degree of lattice distortions inside grains. These colour-coded maps show the change in crystal orientation with respect to its average orientation. Lattice distortions within deformed grains were quantified by calculation of the local dislocation density using the ‘Weighted Burgers vector’ (WBV) analysis following the approach described by Wheeler *et al.* (2009, 2024) and Timms *et al.* (2019). Specifically, we performed a loop around the area of titanite grains where the LA-ICP-MS spot analyses were taken. The derived dislocation density value refers to the number of geometrically necessary dislocations that are needed to accommodate the measured lattice distortion over the area in which the LA-ICP-MS spot was taken.

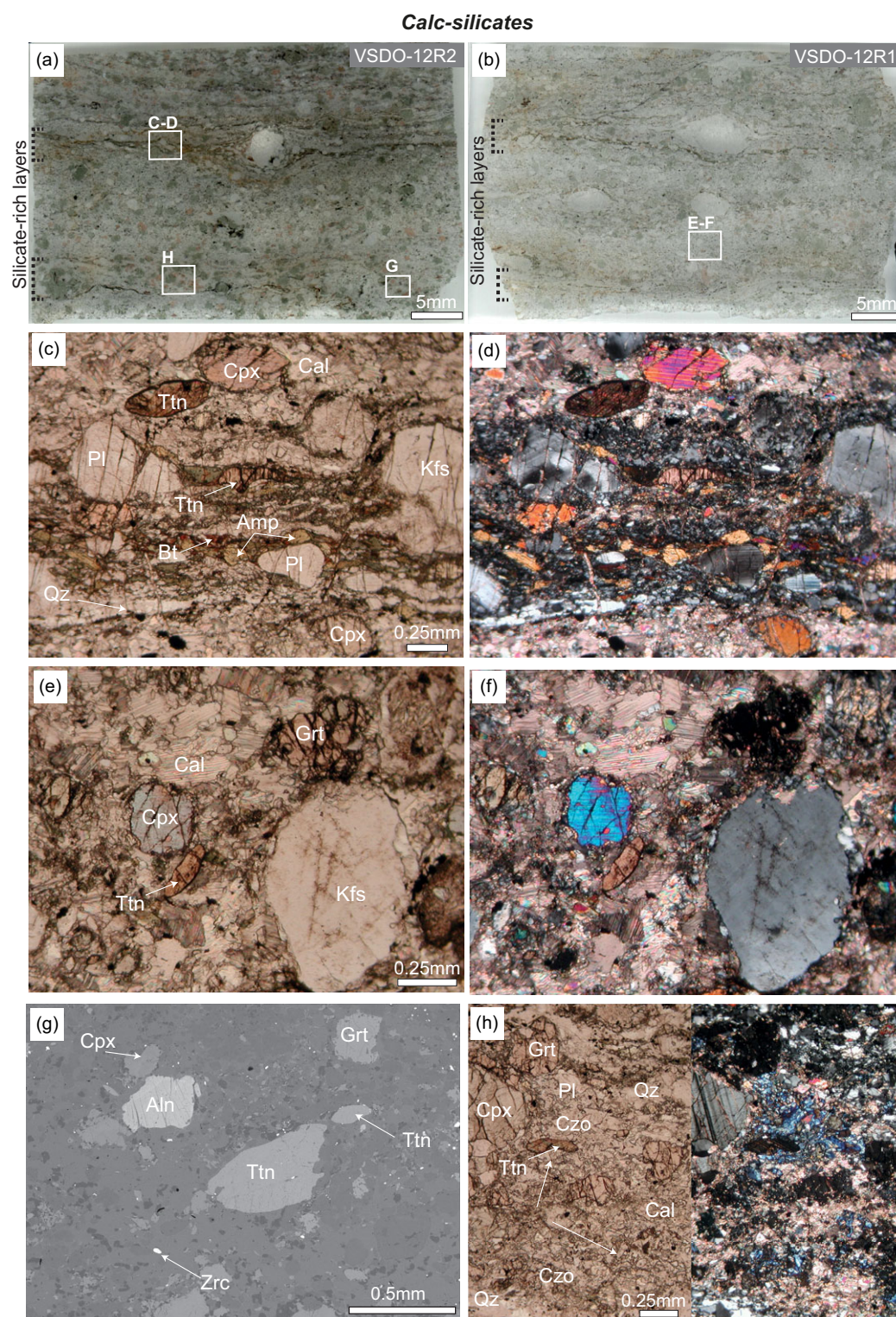


Figure 3. Thin-section scans (a-b) of sheared calc-silicates with thin silicate-rich layers highlighted by the dashed bracket on the left side of each image. Microphotographs show the main petrographic and textural features under both plane (c, e) and crossed (d, f) polarized lights of calcite-poor (c, d) and calcite-rich layers (e, f). The BSE image in g highlights the presence of a large allanite grain close to titanite. The microphotograph in h shows the occurrence of retrograde clinozoisite under both planes (left side) and crossed (right side) polarized lights.

3.d. Monazite and titanite U-(Th)-Pb dating

Monazite and titanite U-(Th)-Pb dating was carried out using a laser ablation, inductively coupled, plasma mass spectrometry (LA-ICP-MS) at CNR-Istituto di Geoscienze e Georisorse U.O. Pavia (Italy). Analytical details, with the technical/methodological parameters following the PlasmaAge recommendation, are reported within Table S3 (Supplementary Material).

The large size of titanite grains/domains allowed us to collect simultaneously trace element concentrations and U-Th-Pb isotopes. Trace element concentrations were calculated using SiO_2 as the internal standard and the concentration of 29.8 wt.%, the average obtained from EMPA analyses. NIST610 was used as primary reference materials, and MKED-1 and TTN150 (Klemme *et al.* 2008) were analysed as quality control. The relative standard deviation for MKED-1 is better than 18% and concentrations are

typically within better than 5% for Zr, Nb, Nd, Sm, Tb, Dy, Ho, Er, Tm, Hf, Th and U; better than 11% for Al, Ti, Mn, Fe, Pr, Eu, Gd, Yb, Lu and Pb of expected values for 'MKED-1' (Spandler *et al.* 2016). Vanadium, Y, La and Ce are less accurate (21–13%).

Moacir monazite (Cruz *et al.* 1996; Seydoux-Guillaume *et al.* 2002; Gasquet *et al.* 2010) and MKED-1 titanite (Spandler *et al.* 2016) were used as the primary standards for U–(Th–)Pb dating and were run every ~ 10 unknowns. Precision and accuracy are reported within Table S3 (Supplementary Material).

The software GLITTER[®] was used for data reduction (Van Achterbergh *et al.*, 2001) of both isotopic ratio and trace elements. IsoplotR (Vermeesch, 2018) was used for representing isotopic data of both monazite and titanite; ages are provided together with the 2 σ uncertainties. Monazite data with discordance higher than 5% and/or a spot overlap were excluded to avoid data bias. The $^{238}\text{U}/^{206}\text{Pb}$ and $^{207}\text{Pb}/^{206}\text{Pb}$ isotopic ratios for each analysis are presented uncorrected for common lead in Tera-Wasserburg concordia diagram using IsoplotR (Vermeesch, 2018).

Full analytical results for monazite and titanite are reported as Supplementary Material Table S4 and S5, respectively.

3.e. Zr-in-titanite thermometer

The Zr-in titanite thermometer of Hayden *et al.* (2008) was used to calculate titanite temperatures. Uncertainties are given at 2 σ , propagated assuming ± 0.1 GPa for pressure estimates, 2 σ variation of the Zr concentration in titanite and the 2 σ uncertainties given by the authors for their calibration of the thermometer (see Cruz-Urbe *et al.* 2014). Temperature estimates are reported in Table S5 (Supplementary Material).

4. Field observations and general petrography

The Forno-Rosarolo Shear Zone (FRSZ), also known as Rosarolo Shear Zone (Siegesmund *et al.* 2008), crops out in the IVZ section of the Strona di Omegna valley between the Rosarolo and Forno villages (Figure 1b). It was recently mapped and characterized in detail by Simonetti *et al.* (2023). It is a NE-SW-oriented shear zone with a thickness of about 500m. Mylonitic foliation is subvertical, in places steeply dipping toward the NW. A sinistral top-to-the-SW sense of shear is well highlighted by the presence of δ - and σ -type porphyroclasts, shear boudins, flanking structures and winged inclusions in all the involved lithologies (Simonetti *et al.* 2023). The FRSZ developed in a narrow area described as the transition zone between the amphibolite- and granulite-facies metamorphic rocks (Redler *et al.* 2012; Kunz *et al.* 2014). Several lithologies are involved in the deformation, in particular paragneisses, metabasites and local calc-silicates (Simonetti *et al.* 2023). The margins of the shear zone are characterized by two low-strain domains (Figure 1b), with different thicknesses, made by anastomosed protomylonites and mylonites layers surrounding weakly deformed lenses, whereas the high-strain core (Figure 1b) consists of alternating mylonites and ultramylonites. The sheared rocks are characterized by a foliation-oriented NE-SW and dipping at variable angle, between 42° and 88°, toward the NW and a mineral lineation plunging at moderate angle toward the NE (Figure 1b).

The protomylonitic biotite-poor paragneiss is coarse grained and consists of quartz, feldspars, sillimanite, garnet and minor biotite (Figure 2a). Rutile, zircon, monazite, oxides and sulphides are accessories. Intracrystalline deformation is recognizable in all major phases. Feldspars show undulose extinction and deformation lamellae, they are only locally fractured, and biotite shows

kinks of the cleavage. Quartz is coarse-grained and presents lobate grain boundaries and window and pinning structures. Sometimes chessboard extinction microstructure is also present. Locally, quartz-rich domains are characterized by a gradual grain-size reduction and by the presence of both subgrains and new grains forming a 'core and mantle structure' around larger grains. The prismatic sections of sillimanite show undulose extinction. These rocks are affected by intense fracturing and veining at high angles with respect to the foliation. Fractures and veins are generally closely spaced and crosscut the grains. This late brittle event promoted the replacement of the primary assemblage by secondary minerals such as chlorite, white mica, epidote and ilmenite. Monazite occurs in different textural positions: totally or partially enclosed within garnet or sillimanite porphyroblasts (Figure 2d), within or among recrystallized quartz grains. Rarely monazite shows jagged contours as evidence for partially replaced by allanite (Figure S1, Supplementary Material) but locally it is affected by intense fracturing.

Protomylonitic biotite-rich paragneisses are characterized by biotite, sillimanite, garnet, feldspars and quartz (Figure 2b,e). Monazite, zircon, rutile and graphite are common accessories. These paragneisses show a migmatitic texture overprinted by a well-defined foliation marked by layers of elongated biotite and large sillimanite prisms with subordinate quartz-feldspathic layers (Figure 2b, e). This foliation wraps around rounded to elliptical garnet grains which contain numerous inclusions of matrix-forming minerals (Figure 2b, e).

Feldspars generally show evidence of ductile deformation such as undulose extinction and deformation lamellae. Quartz is coarse-grained and presents lobate grain boundaries. Locally window and pinning structures and deformation lamellae can be recognized. Some grains also display chessboard extinction microstructure.

Sillimanite prisms show undulose extinction and deformation bands whereas the cleavage of biotite is kinked. Sillimanite fish, asymmetric mantled porphyroclasts and S-C-C' fabric occur indicating a sinistral top-to-the-SW sense of shear. Brittle features are rare as well as the occurrence of secondary minerals such as chlorite after biotite and garnet, ilmenite after rutile.

Mylonitic paragneisses from the high-strain zone show the same mineral assemblage of those from the low-strain zone but differ for a more apparent mylonitic fabric (Figure 2c,f). The foliation is marked by alternating melanocratic and leucocratic layers. The formers are made mainly of biotite and sillimanite whereas the leucocratic ones consist of quartz and feldspars (Figure 2c,f). As porphyroclasts, we observed mainly garnet, sillimanite and feldspars. Garnet occurs as rounded or elongated grains parallel to the foliation and, compared to less deformed rocks, it experienced an apparent grain-size reduction (Figure 2c,f). Sillimanite occurring in basal section commonly forms fish-shaped porphyroclasts rarely replaced at the edges by retrograde white-mica. The prismatic sections are generally elongated parallel to the foliation and show evidence for both ductile deformations, such as undulose extinction and kinking, and brittle deformation such as necking and fractures. Also in these samples, monazite is rarely partially replaced by allanite growing syn-kinematically (Figure S1, Supplementary Material).

Calc-silicates are well exposed in a small outcrop along the river (Figure 1b). They are characterized by large (up to few centimetres) whitish clasts containing feldspars and mafic minerals (clinopyroxene and amphibole) surrounded by a greyish fine-grained matrix (Figure 3a,b). At the microscale, they show a well-developed foliation and mylonitic fabric (Figure 3a–h). The largest

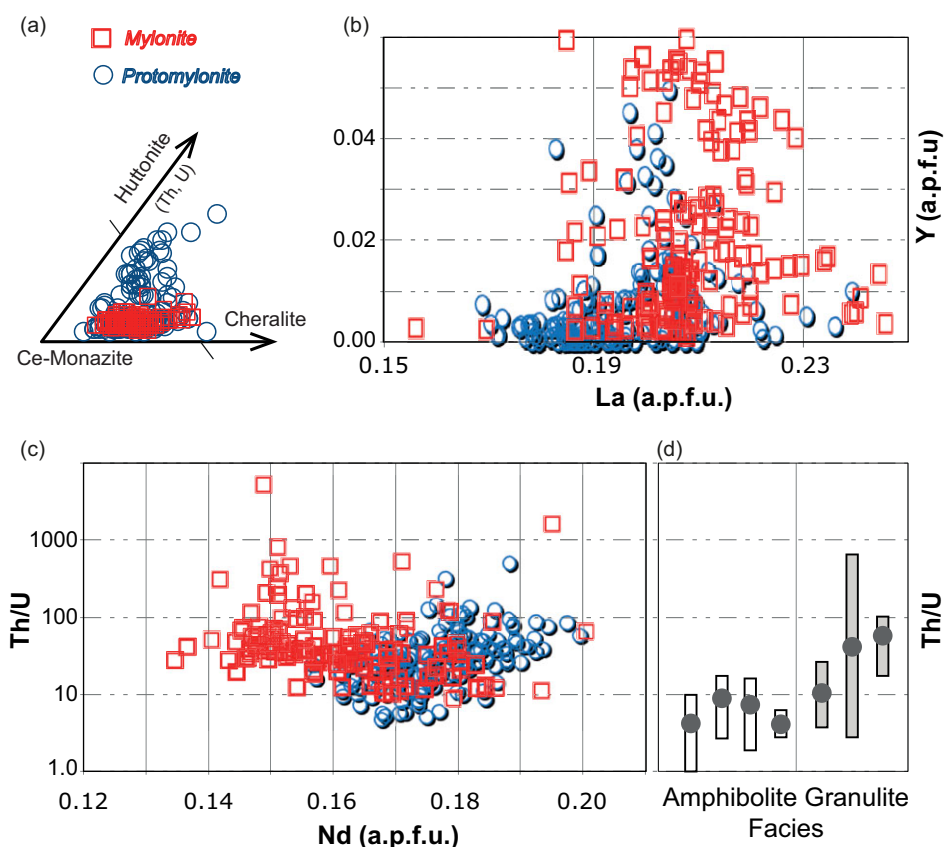


Figure 4. Mineral chemistry of monazite from mylonites (red squares) and protomylonites (blue circles). (a) Monazite composition and classification according to Linthout (2007), (b) Y (a.p.f.u.) versus La (a.p.f.u.), (c) Th/U versus Nd (a.p.f.u.). (d) Th/U ratio of monazite from metasedimentary rocks with different metamorphic degrees from the Valle Strona di Omegna after Williams et al. (2022).

porphyroclasts are made of feldspars whereas clinopyroxene and garnet are smaller (Figure 3a–h). Calc-silicate shows a compositional layering consisting of calcite-rich layers alternating with layers richer in silicates (Figure 3a,b). The latter are generally thinner and are made of plagioclase, quartz, green-amphibole and biotite with rare or minor calcite (Figure 3c,d). Due to the low modal abundance of calcite, they can be defined as carbonate-bearing calc-silicate layers. The thicker calcite-rich layers contain (sub)rounded to elliptical grains of clinopyroxene and feldspars; anhedral garnet, locally showing a poikiloblastic texture, is also common (Figure 3e–h). Titanite is an abundant accessory mineral whereas allanite and zircon are less common (Figure 3g). Feldspars and clinopyroxene show evidence for intracrystalline deformation such as undulose extinction; deformation twins are well recognizable within plagioclase (Figure 3d,f,h). Thin ribbons of recrystallized quartz are also common in the carbonate-bearing calc-silicate layers (Figure 3d,h). Features indicative of brittle deformation are also common: major minerals as well as titanite and allanite show fractures, locally associated to a small displacement of fragments. Fractures are filled by secondary minerals such as calcite, chlorite and epidote. Retrograde replacement of primary mineral assemblage is not only localized along fractures; within the calcite-poor layers, clinozoisite is abundant and generally replaces feldspars.

5. Monazite

5.a. Monazite composition

We identified a total of 32 monazite grains in the biotite-rich paragneisses and 4 monazite grains in the biotite-poor paragneisses (Table S6, Supplementary Material). The results of EPMA

analysis are reported in Table S1 (Supplementary Material). The monazite grains analysed are rare earth element (REE) phosphate with Ce as the dominant REE (Figure 4) and thus they can be classified as monazite-(Ce) according to Linthout (2007). Monazites from protomylonites are characterized, on average, by a higher huttonite component (Figure 4) due to the increase of Th and U with respect to Ca + Si following the solid solution between cheralite ($\text{Ca}(\text{Th,U})(\text{PO}_4)_2$) and huttonite $(\text{Th,U})\text{SiO}_4$ end-members (Förster, 1998; Linthout, 2007).

Among the analysed elements, Nd, Y and La show apparent variations as function of the rock fabric. While Y and La are on average higher within monazite from mylonites, Nd has an opposite trend (Figure 4b–c; Table S1, Supplementary Material). The Th/U ratio does not change significantly within the two different sheared rocks (Figure 4c; Table S1, Supplementary Material) and it has values comparable to those reported for monazite within granulites exposed in the Valle Strona di Omegna (Williams et al. 2022; Figure 4d).

5.b. Monazite textural position and zoning

5.b.1. Protomylonite: Biotite-poor paragneiss (VSDO-13B1)

Here, we selected 4 monazite grains (Mnz1a, Mnz4a, Mnz6a and Mnz6b) that are among grains of major rock-forming minerals or included within a sillimanite porphyroblast (Figure 5, Table S6, Supplementary Material).

Mnz1a and 6b have an elongated shape whereas Mnz6a has a more irregular shape with cusate terminations. All these grains are characterized by a large Th-rich core surrounded by thin rims/edges with lower Th content. Y is generally homogeneous within the large core and tends to be higher in the outermost domains (a few μm) of the grains (Figure 5a–b). Mnz4a is stubby (Figure 5b)

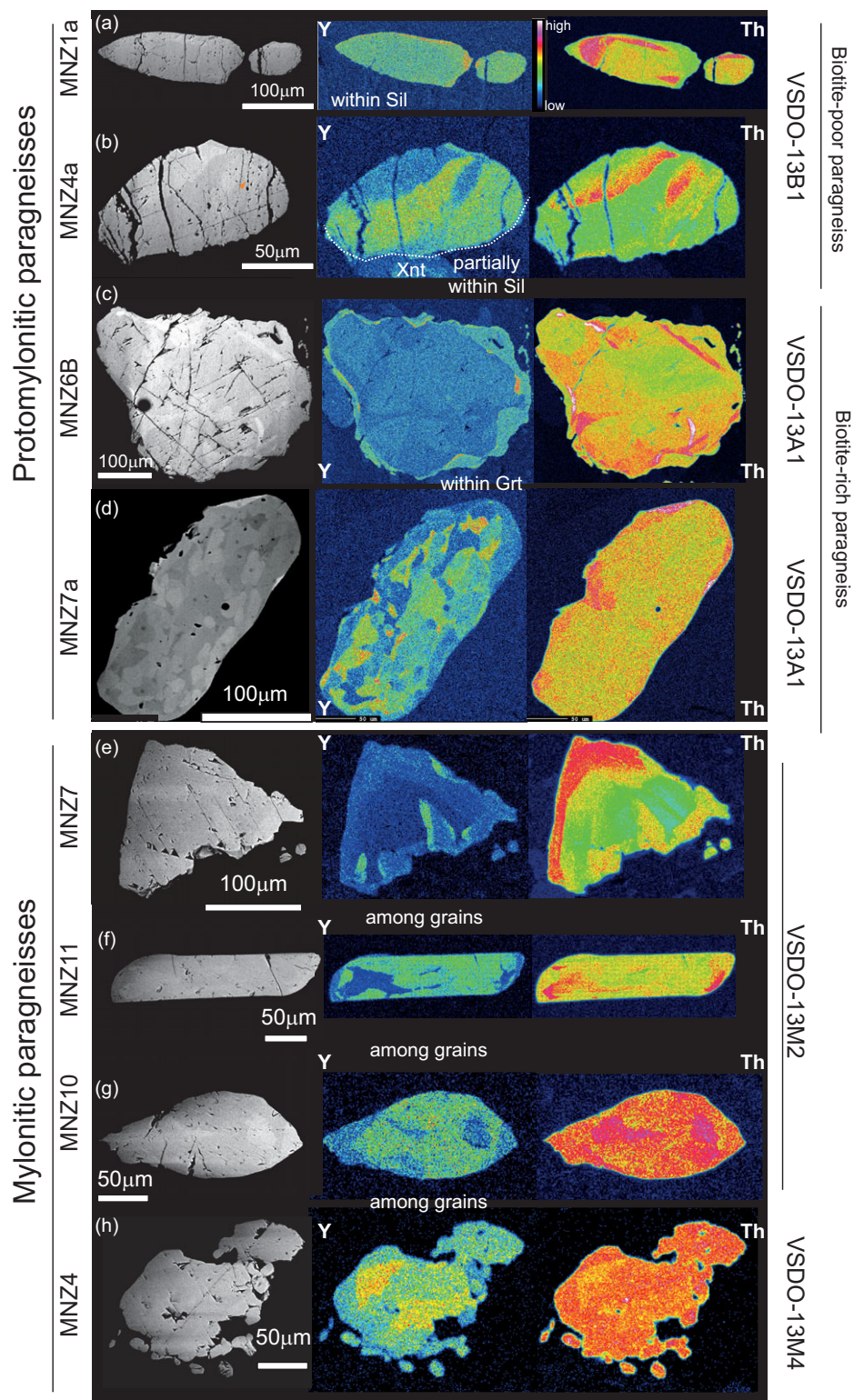


Figure 5. BSE and chemical X-ray maps (Y, Th) of monazite grains within proto- and mylonitic paragneisses (a-h). The textural position of each monazite grain is reported within the Y-map. The locations of monazite in A and B are reported in Figure 2d, and the locations of monazite grains in d and f are shown in Figure 2e,f, respectively.

and differs from the other grains since it shows opposite zoning features: on one side, towards the foliation, high-Th and low-Y domains occur. This grain is also characterized by intense fractures that crosscut the entire grain, and it has numerous fine-grained pores/inclusions aligned almost parallel to the main fractures (Figure 5b).

5.b.2. Protomylonite: Biotite-rich paragneisses (VSDO-13A1)

In sample VSDO-13A1, a total of 9 grains were characterized by X-ray maps: 8 grains are located along the main foliation and 1 is included in garnet (Table S6, Supplementary Material).

The monazite grains located along the main foliation show a variable size and shape (Table S6, Supplementary Material), and all

present apparent chemical zoning for Y and Th (Figure 5a–d and Figure S2 and Table S1, Supplementary Material). The most common zoning pattern consists of large cores richer in Th and poorer in Y surrounded by thinner irregular rims richer in Y and poorer in Th (e.g. Mnz6b Figure 5c and Mnz2a, 8a, Figure S2). The Th distribution in the internal domains is irregular and locally reaches concentrations up to 12wt.% (ThO₂). Locally Y-rich bands alternate with Th-rich ones (e.g. Mnz4a, Figure 5b). Monazite grains totally or partially enclosed within garnet are characterized by patchy zoning of both Y and Th (e.g. Mnz7a, Figure 5d). Less commonly, Y is almost homogeneously distributed within the grain whereas Th looks oscillating (e.g. Mnz1a Figure 5a).

5.b.3. Mylonites: paragneisses

Sheared paragneisses (VSDO-13M1, VSDO-13M2 and VSDO-13M4) contain abundant monazite grains. Twenty-three grains were selected as representative of different textural positions and were fully characterized (EPMA chemical analyses and X-ray maps; Table S1, Supplementary Material): 13 are located along the main foliation, 3 are in the strain shadow around porphyroclasts, 4 are in contact with garnet and 3 are totally or partially included within garnet porphyroclasts (Table S6, Supplementary Material). Some of these monazite features are shown in Figure 5 and S2. The X-ray maps of selected monazite grains revealed that monazite shows three main different zoning patterns.

(i) Ten of the analysed twenty-three grains do not show a clear core-rim zoning and are locally characterized by internal domains poorer in Y and external domains richer in Y (e.g. Mnz7, VSDO-13M1; Mnz7 VSDO-13M2; Mnz14, VSDO-13M4, Figure 5e). In these grains, Y and Th are correlated.

(ii) Seven of the analysed twenty-three grains show irregular shapes with inner domains richer in Y and external domains Y-depleted. In these grains, the zoning pattern of Th is not apparently correlated with Y (e.g. Mnz6, VSDO-13M1; Mnz4 VSDO-13M4, Figure 5h).

(iii) Five of the analysed twenty-three grains are elongated (high aspect ratio) and show richer Y cores and poorer Y rims/tips (Mnz15, Mnz11 and Mn10 VSDO-13M2, Figure 5f–g). Also in these grains, the zoning pattern of Th is not apparently correlated with Y.

A patchy distribution of both Th and Y was observed for one grain partially included within garnet (e.g. Mnz15, VSDO-13M4).

5.c. Monazite quantitative orientation data

Four monazite grains from the studied samples were analysed by EBSD (Figure 6). Two from the protomylonitic paragneiss (Mnz2a, Mnz6B, VSDO-13A1) and two from the mylonitic paragneiss (Mnz1, Mnz2, VSDO-13M1). All monazite grains show significant distortions (up to 12°) regardless of the degree of strain intensity of the two different samples. However, monazite grains from mylonites show a higher degree of distortions strongly localized at the rims/tips of the grain with respect to those from protomylonites. In all grains, the systematic orientation of the main grain (blue colour) with little changes of distortions towards the rims (red colour) is highlighted not only by EBSD maps but also by the profile and pole figures (Mnz2a, Mnz2; Figure 6a,d). The single blue points in pole figures emphasize the occurrence of neoblasts (e.g. Mnz6B, Mnz1; Figure 6b,c).

Monazite from the protomylonite (VSDO-13A1) shows slightly continuous and discontinuous increasing lattice distortions from core to rim (around 5–8°; Figure 6a,b). In these grains, the higher

degree of distortion is focused on the rim/tips (Mnz2A; Figure 6a) and where the changes in orientation are due to the occurrence of grain boundaries (Mnz6B; Figure 6b).

Monazite from the mylonite (VSDO-13M1) presents significant lattice distortions especially focused on the rim/tips (up to 12°; Figure 6c,d). The accumulation of distortions locally develop into distinct neoblasts (Mnz1; Figure 6c).

5.d. Monazite U–Th–Pb dating

5.d.1. Protomylonites

A total of eighty-eight analyses were performed on 12 monazite grains within the protomylonites (4 grains from the biotite-poor sample; Figure 7a–b; Table S4, Supplementary Material). Sixty-three data resulted concordant (% of concordance >95%) for both ²⁰⁶Pb/²³⁸U vs ²⁰⁷Pb/²³⁵U and ²⁰⁶Pb/²³⁸U vs ²⁰⁸Pb/²³²Th systematics in the range of 314±6 Ma to 184±6 Ma. The dominant Carboniferous–Permian dates (57% of the total dataset) were obtained mostly from cores of monazite occurring within the foliation and from one grain enclosed within garnet. These grains are characterized by both cores to rim zoning features (low-Y cores or inner domains surrounded by high-Y rims and/or external domains) or patchy zoning (Figure 7b, Figure S3). The Triassic data (33% of the total dataset) were obtained mostly from high-Y external portions (Figure 7b) whereas the youngest Jurassic dates were obtained from one high-Y grain occurring as satellite around a larger grain (Figure S3), a high-Y rim of a monazite with patchy zoning and a Y-rich domain of a grain showing numerous fractures and pores (e.g. Mnz4a, VSDO13-B1).

5.d.2. Mylonites

A total of eighty-eight analyses were performed on 21 monazite grains within the mylonites (Figure 7a–b; Table S4, Supplementary Material). Sixty-one ²⁰⁶Pb/²³⁸U data resulted concordant (% of concordance >95%) with respect to both ²⁰⁷Pb/²³⁵U and ²⁰⁸Pb/²³²Th data. Although dates show a huge spread from 290 ± 14 Ma to 188 ± 6 Ma they fall mostly in the Triassic period (36 data, 59% of the entire dataset). The minor Carboniferous–Permian dates (8 data, 13% of the entire dataset) were obtained mostly from cores of monazite occurring within the foliation and from two grains partially or totally enclosed within garnet. These grains are characterized by both cores to rim zoning features (low-Y cores or inner domains surrounded by high-Y rims and/or external domains) or patchy zoning. The Triassic and Jurassic dates (53 data, 87% of the entire dataset) were obtained from high-Y rims surrounding low-Y cores and from high-Y elongated or anhedral grains along the foliation (Figure 7b, Figure S4).

6. Titanite

6.a. Titanite textural position

Titanite is found generally as elongated grains aligned with the foliation (Figure 8) with dimensions up to 600x250 µm. Locally, small grains occur as satellites around larger titanite grains (Figure 8a,b). Rarely titanite is observed within clinopyroxene porphyroclasts (e.g. Ttn11; Figure 8h). Two sets of fractures were observed within titanite (Figure 8), one set is parallel to the cleavage and the second one is generally at high angle with respect to the foliation and crosscut the entire grains. In this latter case, fractures are filled by secondary minerals such as chlorite, albite, epidote and ilmenite. As inclusions titanite can host feldspars, calcite, chlorite,

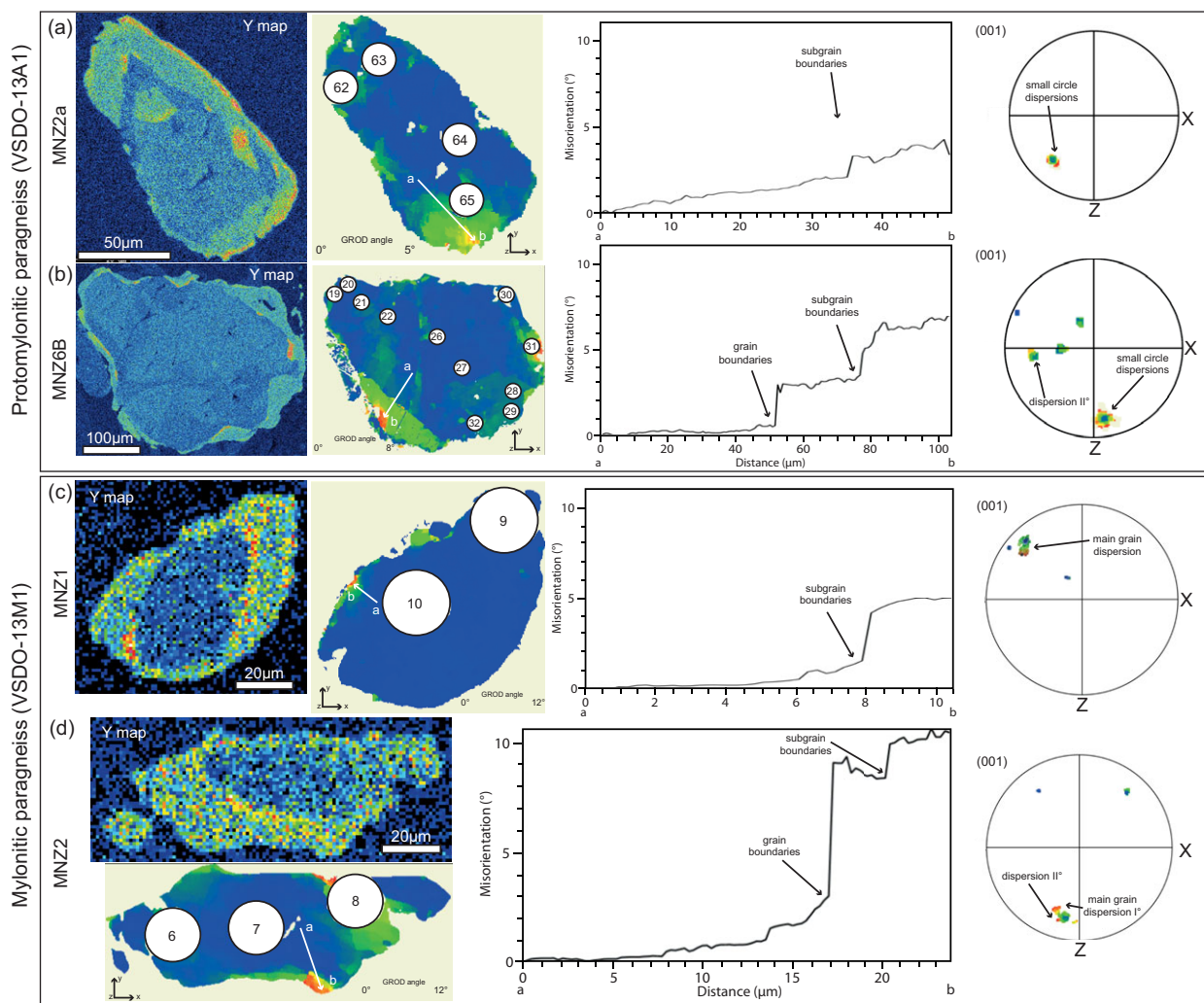


Figure 6. Representative Y maps and microstructural features of monazite within protomylonitic (a, b) and mylonitic (c, d) paragneisses. Microstructural features are shown as relative crystallographic orientation maps (GROD angle map), misorientation profile diagrams (from the point 'a' to 'b', reported in the GROD angle map as white arrow) and pole figure plots for (001) to highlight degrees of distortion across the monazite grain. The numbered white circles on the GROD angle maps represent the LA-ICP-MS spot locations performed on monazite grains numbered according to the U-Pb analyses reported in Supplementary Material Table S4. It is interesting to note that there is no overlap between Y-zoning and increasing distortions. Both maps and plots show the increasing distortions focused on the rim/tips of the grains. Pole figures are plotted in the lower hemisphere, equal area projections in the sample x-y-z reference frame. The colours of point in pole figures reflect the colours of the GROD angle map. Black arrows highlight the way of dispersions.

epidote, apatite, zircon and rarely rutile. Trails of small inclusions/pore are also common (Figure 8).

6.b. Titanite zoning, chemistry and thermometry

Based on textural and chemical features, titanite can be subdivided in two main types. Type 'Z' titanite is apparently zoned in BSE images with darker tips/terminations and brighter cores (Figure 8a–d). Rarely, the darker domains are more extended, partially enveloping the grain (Figure 8b–d). Locally, zoning features are crosscut by brighter parallel bands reflecting twins (Figure 8b–d). Type 'Z' titanite occurs generally within the silicate-rich layers. Type 'unZ' titanite is relatively unzoned in BSE images (Figure 8e–g) and occurs mostly within the calcite-rich layers. Both types can coexist within the same textural site within a distance of a few microns (Figure 8g,h) at the boundary between the two compositional layers (i.e. calcite-rich and silicate-rich layers). The apparent chemical differences between the two types of titanite have been further documented by X-ray maps of both types (Figure

S5 and S6). According to the X-ray maps of two selected grains of type 'Z' titanite, large cores with higher La_2O_3 , Ce_2O_3 and Nd_2O_3 and Nb_2O_5 are surrounded by thinner rims/tips with lower REE (Figure S5). The distribution of elements within the cores is indicative of a sector zoning.

Quantitative chemical analyses of titanite are reported in Supplementary Material Table S2 and Figure 9a–b. Type 'unZ' titanite grains have on average lower TiO_2 (35.9 ± 0.7 wt.%) and Fe_2O_3 (0.34 ± 0.04 wt.%) contents with respect to zoned titanite ($\text{TiO}_2 = 36.6 \pm 0.6$ wt.%; $\text{Fe}_2\text{O}_3 = 0.39 \pm 0.05$ wt.%) and higher Al_2O_3 content (2.5 ± 0.3 vs 2.0 ± 0.3 wt.%; Figure 9a). The CaO content of type 'Z' titanite is highly scattered and on average lower (27.8 ± 0.5 wt.%) than the CaO content of unzoned titanite (28.2 ± 0.2 wt.%; Figure 9b). Analogously, fluorine is on average higher for the type 'unZ' titanite with respect to type 'Z' (0.76 ± 0.07 vs 0.59 ± 0.07 wt.%; Figure 9b).

Fourteen titanite grains were analysed for trace element composition confirming significant differences between the two types of titanite (zoned vs unzoned) and from core to rims of zoned

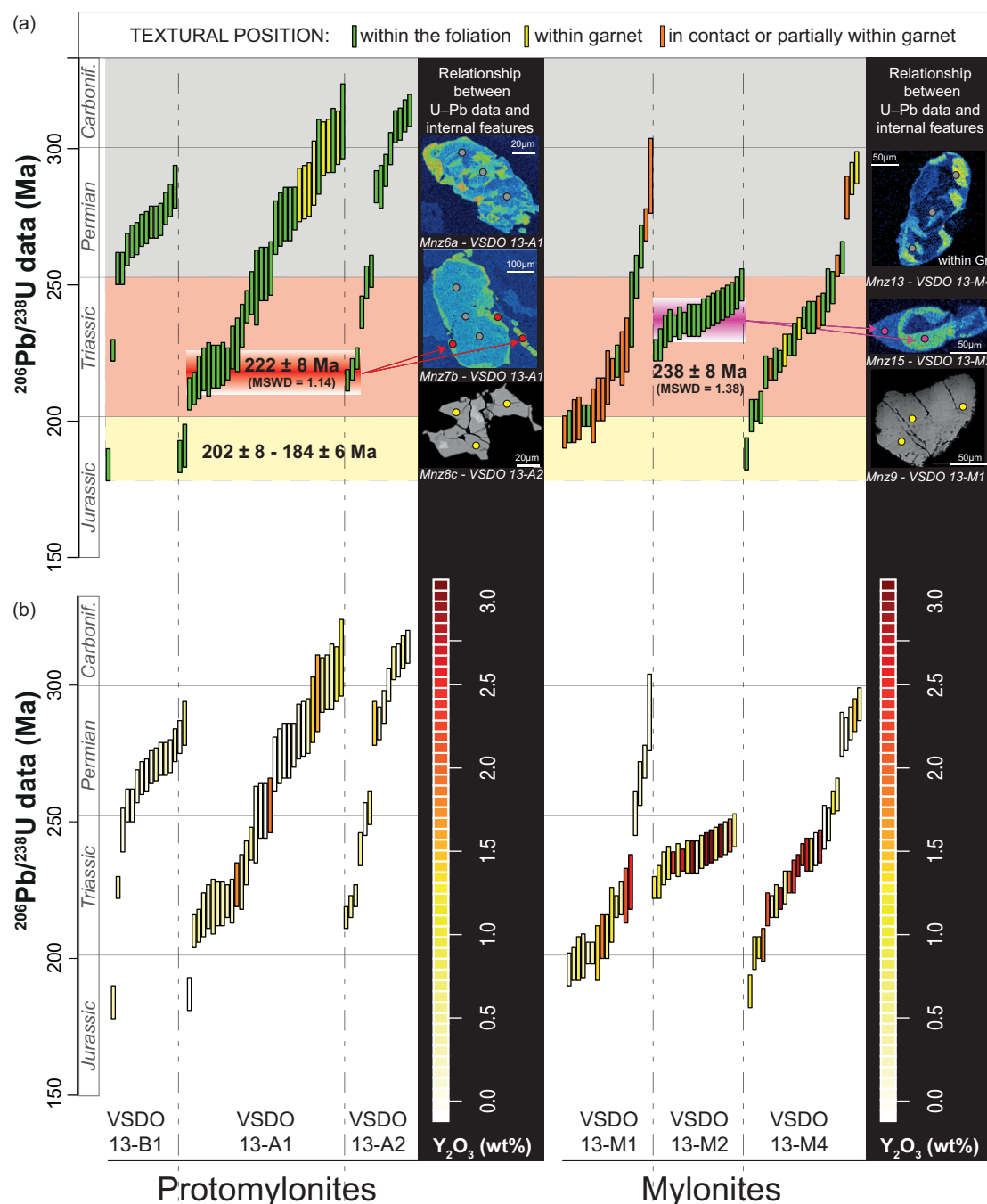


Figure 7. Summary of concordant monazite U–Th–Pb data for protomylonitic and mylonitic paragneisses organized in ascending order for each sample. The length of boxes represents the apparent ages with the 2σ uncertainty. Data are coloured as function of the textural position (a) and the Y content of the relative analytical spot (b). The weighted average of two clusters obtained from specific grains/domains is also reported in (a). The location of the analytical spots for some representative grains is shown on the X-ray maps and BSE images.

titanite grains. The normalized REE patterns reveal that the two different types of titanite show similar trends with LREE fractionated over HREE (Figure 9c–d). This is particularly apparent for type ‘Z’ titanite (Figure 9c), and one type ‘unZ’ grain characterized by a significant depletion of HREE (e.g. Ttn23; Figure 9d). Type ‘Z’ titanite differs also for a more pronounced negative Eu anomaly that is weak or absent for homogeneous titanite (Figure 9c,d). Type ‘Z’ titanite grains are characterized also by a more pronounced intragrain variation of the REE patterns (Figure 9c). Generally, the dark external domains have LREE lower

than 10000 times CI whereas the bright inner domains have LREE higher than 10000 times CI (Figure 9c,e).

Zirconium has an opposite trend with respect to REE (Figure 9e) being on average higher within inner domains of type ‘unZ’ homogeneous titanite grains with respect to type ‘Z’ titanite ($Zr < 1600$ ppm). This difference is much more apparent for the dark external domains of type ‘Z’ titanite where Zr is < 500 ppm (Figure 9e). The two types of titanite are well distinguishable in terms of Nd contents. The type ‘unZ’ grains are generally poorer in Nd (< 1000 ppm) with respect to type ‘Z’ titanite (Figure 9e).

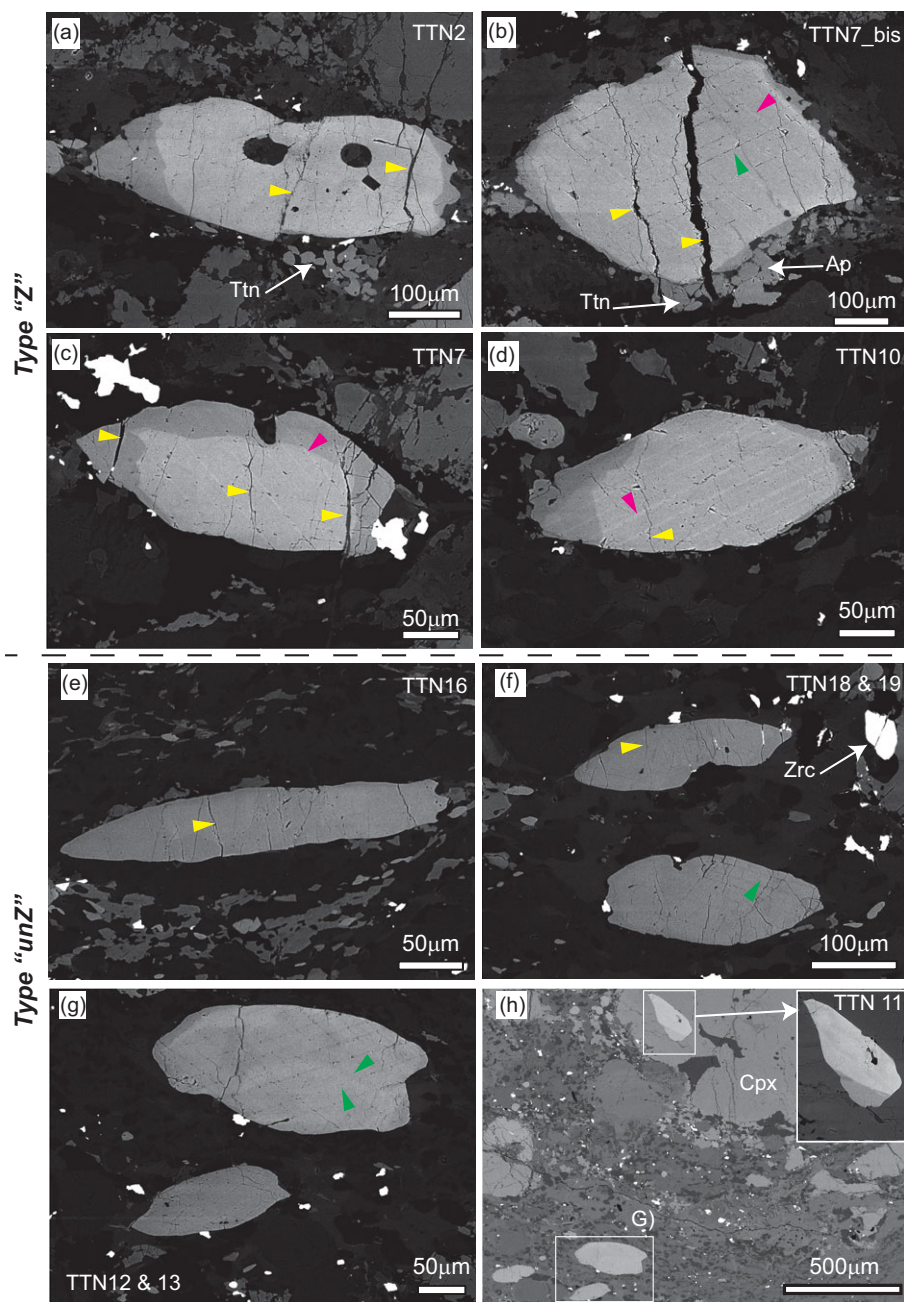


Figure 8. High contrast BSE images of titanite within calc-silicates showing textural and internal features. (a–d) Type ‘Z’ (Zoned) titanite consisting of large brighter cores surrounded by thin darker asymmetric rims. Small titanite grains occurring as satellites close to the large grains are shown in a and b. (e–g) Type ‘unZ’ (unzoned) titanite without apparent zoning. In both Types, fractures (yellow arrows) at high angle with respect to the foliation are common. Two sets of twins are highlighted by green and purple arrows and are more pronounced within the Type Z titanite. (h) BSE Image of a textural site showing the location of titanite grains within the matrix reported in (g), and a grain included within a clinopyroxene porphyroclast. The inset is the high-contrast BSE image of this included grain.

By adopting the Zr-in-titanite thermometer of Hayden *et al.* (2008), the obtained temperatures range from 741 to 866°C for type ‘Z’ titanite and from 744 to 919°C for type ‘unZ’ titanite. The external domains of both types of titanite are systematically poorer in Zr content and thus provide lower temperatures with respect to the internal domains (Figure 9f). The obtained temperature values overlap the peak temperature conditions estimated from the surrounding metabasite and metapelitic rocks equilibrated under high-grade metamorphic conditions (e.g. Kunz & White, 2019; Figure 9f).

6.c. Titanite quantitative orientation data

Seventeen titanite grains were analysed with EBSD; we present four representative grains in terms of deformation and type (type ‘Z’ Figure 10a–d, type ‘unZ’, Figure 10e–h). Most of the analysed grains

show at least one set of polysynthetic straight to slightly kinked twin lamellae (e.g. Figure 10). The twins have a thickness of about 0.5 μm, cross the grain and terminate against grain boundaries with a disorientation from the host grain by $\sim 74^\circ / \langle 102 \rangle$ in accordance with previous studies (Timms *et al.* 2019; McGregor *et al.* 2021; Corvò *et al.* 2023).

While twins are common for the two studied titanite-type grains (‘Z’ and ‘unZ’), the other deformation features differ between them.

Type ‘Z’ titanite shows lattice distortions up to 21° focused to rims/tips (10 grains; ttn2, ttn4, ttn5, ttn7, ttn10, ttn23, ttn24, ttn34, ttn27 and Ttn40; Figure 10a–d), whereas type ‘unZ’ titanite has diffuse and weak ($< 5^\circ$) intracrystalline lattice distortions (six grains; ttn18, ttn19, ttn3, ttn16, ttn25 and ttn26; Figure 10e–h). One exceptional elongated grain (ttn17) exhibits fragmented (domino-like) texture with stepped variation of the distortion

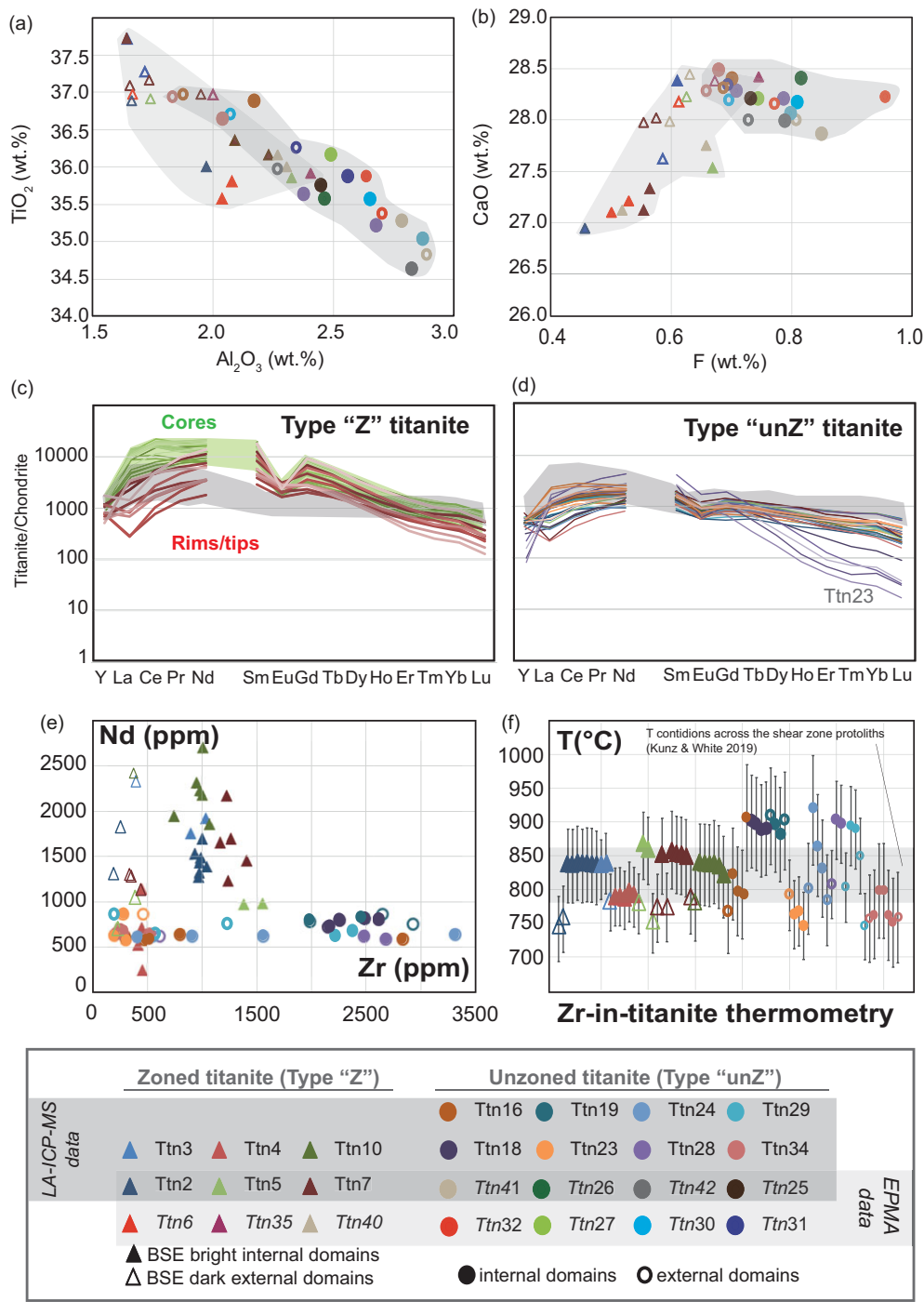


Figure 9. Diagrams of titanite chemistry showing the differences between the two main Types. (a) TiO₂ (wt.%) vs Al₂O₃ (wt.%), (b) CaO (wt.%) vs F (wt.%). The grey areas enclose the data from the two Types. (c) and (d) Chondrite-normalized REE patterns of Type 'Z' and 'unZ', respectively (chondrite values from McDonough & Sun, 1995). For comparison, the Chondrite-normalized REE patterns of titanite grains from sheared amphibolite and calc-silicate layers from the Anzola Shear Zone are reported in grey (Corvò et al. 2023). (e) Nd (ppm) vs Zr (ppm), (f) Temperature (°C) estimate according to the Zr-in-titanite thermometry (calibration of Hayden et al. 2008). The grey shaded box indicates the Temperature conditions for the regional metamorphism obtained by Kunz & White (2019) with P-T pseudosection calculations for unshredded metabasic and meta-pelitic rocks at the boundary of the shear zone.

angle and minor subgrains (Figure 10h). Quantification of the local dislocation density (measured as Weighted Burgers vector, hereafter WBV) for type 'Z' and type 'unZ' grains provides average values for laser spot analyses of 0.0043 μm^{-1} and 0.0018 μm^{-1} , respectively (Table S5, Supplementary Material). Overall, for both titanite types, deformation and orientation changes do not perfectly overlap the chemical zoning.

6.d. Titanite U-Pb dating

A total of 73 petrochronological analyses were performed on 14 grains within a mylonitic calc-silicate (VSDO-12R2B). Results are

summarized in Supplementary Material Table S5 and Figure 11. The U-Pb data are dispersed on the Tera-Wasserburg diagram defining a large U-Pb field suggesting ternary mixing between different common Pb values and multiple radiogenic Pb components. In order to interpret the U-Pb data, we looked for alignment of the isotopic data correlated with the textural position, chemistry and/or deformation microstructure (i.e. dislocations density) for each titanite type, namely type 'Z' and type 'unZ' (Figure 11).

By considering the average dislocation density calculated for each U-Pb analytical spot, no clear correlations are apparent (Figure 11a,b). A weak correlation with ΣLREE and isotopic data is

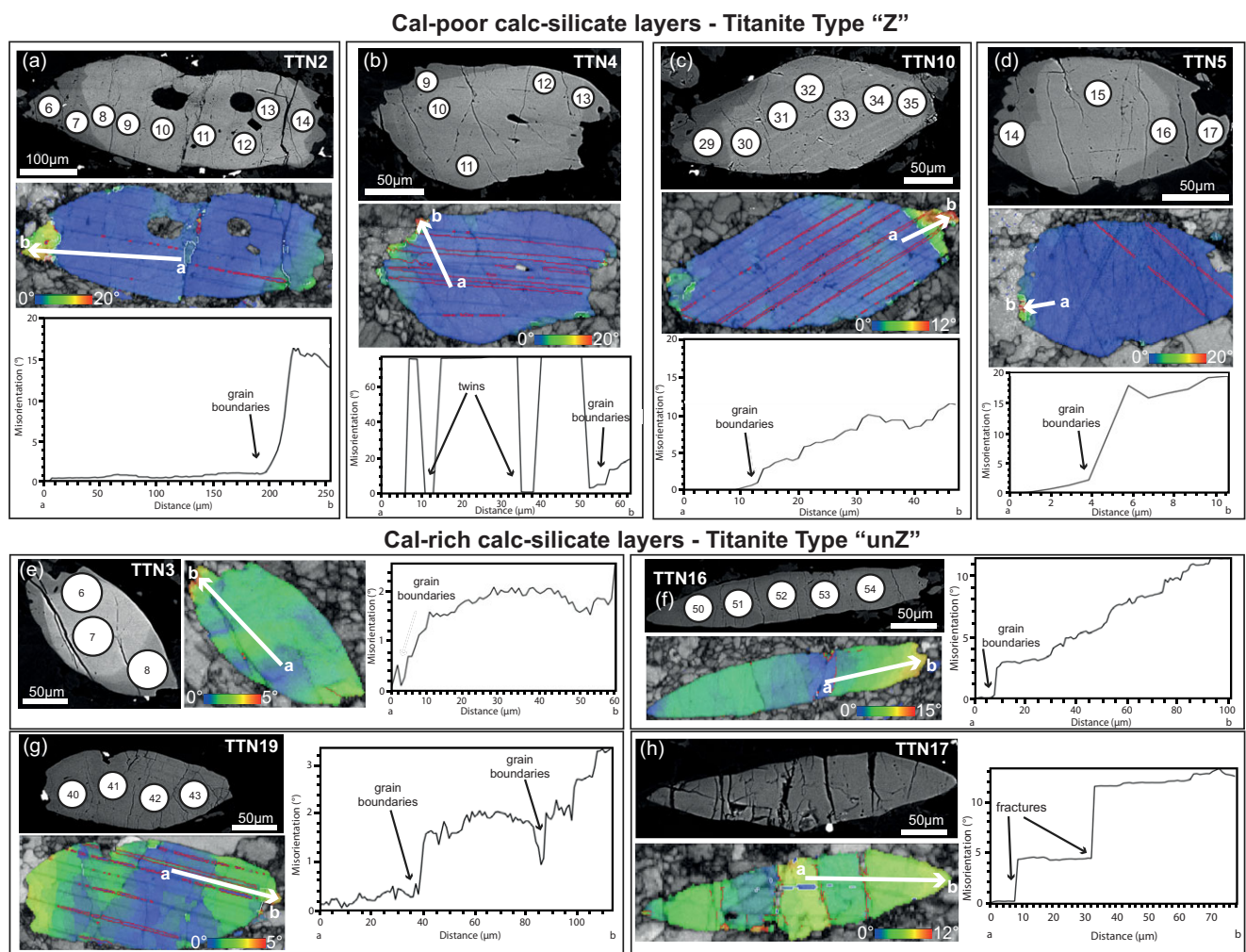


Figure 10. BSE and microstructural features of titanite within calc-silicates (sample VSDO-12R2) in Cal-poor calc-silicates (a-d; Type ‘Z’) layers and Cal-rich calc-silicates (e-h; Type ‘unZ’). Microstructural features are shown as relative crystallographic orientation maps (GROD angle map) and misorientation profile diagrams (from the point ‘a’ to ‘b’, reported in the GROD angle map as white arrow). The numbered white circles on the BSE images represent the LA-ICP-MS spots numbered according to the U–Pb analyses reported in Supplementary Material Table S5. It is interesting to note that there is no overlap between BSE-zoning and increasing distortions. While titanite Type ‘Z’ shows the increase of distortions focused on the rim/tips of the grains, titanite Type ‘unZ’ shows little degree of distortion spread across the whole grain.

appreciable, especially for zoned titanite (type ‘Z’; Figure 11c). The analytical spots collected from domains richer in LREE are generally located to the left of the data population (Figure 11c,d).

The location of the analysis spots shows a slight systematic in the TW diagram (Figure 11e,f): external domains/tips of both types show a good alignment on the TW defining a lower intercept at 186 ± 6 Ma (Figure 11g). The entire dataset is bounded by another regression line mostly coinciding with the innermost domains of both zoned and homogeneous titanite grains. This regression line has a lower intercept age at 240 ± 5 Ma. The U–Pb data between the two regression lines refer to cores and intermediate positions (Figure 11e–g).

7. Discussion

7.a. Behaviour of monazite as function of the deformation fabric

As shown in the Kernel Density Estimation plots of Figure 12a, the distribution of concordant data of monazite grains within

protomylonites ranges broadly from Carboniferous–Permian (52% of the data) to Triassic (48% of the data) with rare Jurassic dates. This spread is partially overlapping the monazite radiometric data from unshered metamorphic rocks collected along the Valle Strona di Omegna crustal section (Figure 12b; Henk *et al.* 1997; Guergouz *et al.* 2018; Williams *et al.* 2022; Wyatt *et al.* 2022). Conversely, the distribution of U–Th–Pb concordant data of monazite grains within mylonites is tighter being almost made by Triassic–Jurassic dates (85% of the data; Figure 12a) which are scarce in previous studies of unshered metamorphic rocks from the same crustal section (Figure 12b).

These different distributions of U–Th–Pb concordant data between monazite from protomylonites and mylonites are correlated with textures, microstructure and chemistry (zoning features). Monazite grains from protomylonites have stubby or rounded shapes (low aspect ratio) and are generally larger with respect to monazite from mylonites (Figure 5, Table S6, Supplementary Material). They are generally characterized by large homogeneous cores surrounded by thin rims with lobate boundaries towards the cores (Figure 5). Conversely, within

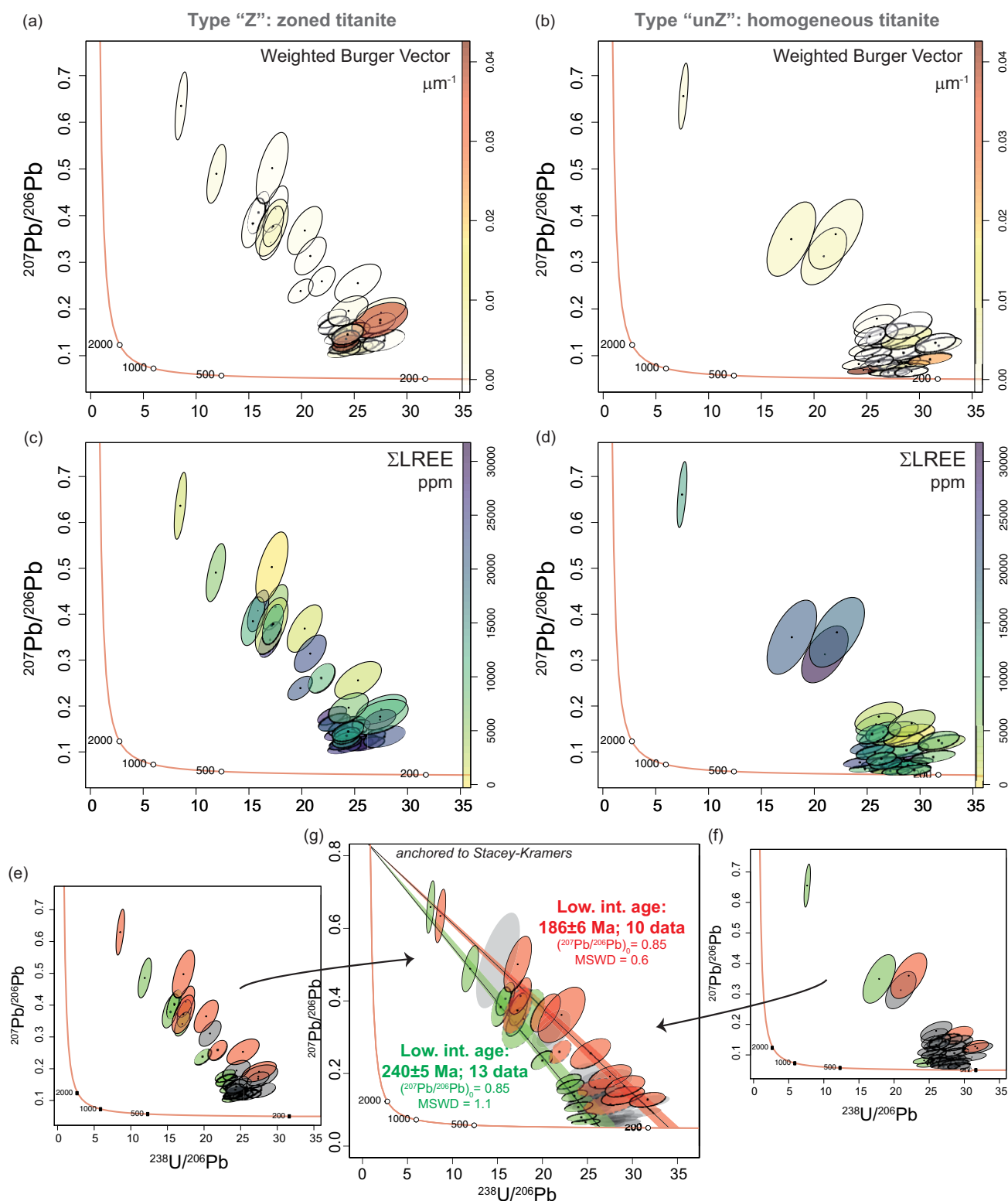


Figure 11. Tera-Wasserburg diagrams of titanite U-Pb data from Type 'Z' (a, c, e) and Type 'unZ' (b, d, f) from sample VSDO-12R2. Each ellipse represents a U-Pb data point and is coloured as function of: the relative microstructure, defined as the Weighted Burger Vector (a, b); the ΣLREE (c, d) and its position within the grain, i.e. core vs rim (e, f). (g) Cumulative Tera-Wasserburg diagram for both titanite types showing the regression lines anchored to Stacey & Kramers (1975) common Pb ratios considering the U-Pb data from the innermost cores (green filled ellipses) and outermost rims/tips (red filled ellipses) of titanite grains. The relative lower intercept ages are also reported. The data points delimited by a dashed line were not included in the calculation of the intercept ages.

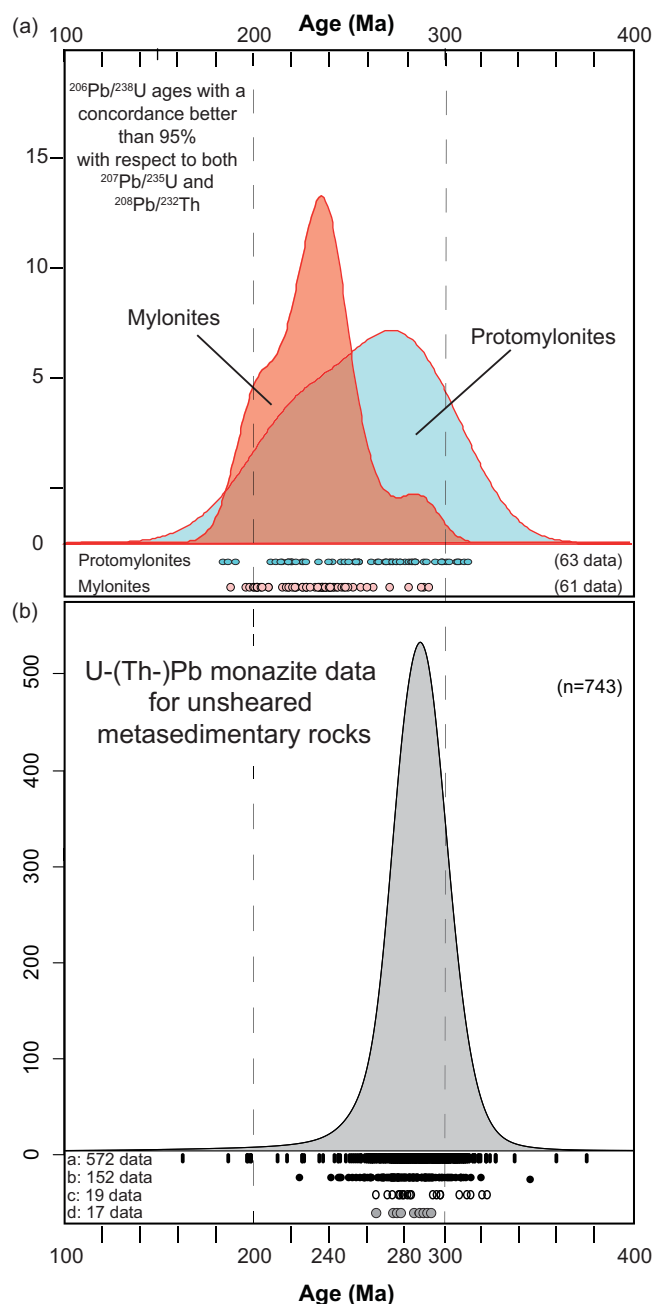


Figure 12. Kernel Density Estimation (KDE) of U-Th-Pb monazite data for sheared (a; this work) and unsheared (b; from literature data) metasedimentary rocks exposed in Val Strona di Omegna. (a) $^{206}\text{Pb}/^{238}\text{U}$ monazite dates for mylonitic (reddish-filled KDE curve and data points) and protomylonitic (bluish-filled KDE curve and data points) samples. Data points (small circles below the curve) in (b) refer to: (a) $^{208}\text{Pb}/^{232}\text{Th}$ monazite dates from amphibolite- to granulite-facies metasediments, after Wyatt *et al.* (2022); (b) $^{206}\text{Pb}/^{238}\text{U}$ corrected monazite dates from amphibolite- to granulite-facies metasediments, after Williams *et al.* (2022); (c) $^{207}\text{Pb}/^{206}\text{Pb}$ monazite data from amphibolite-facies metasediment, after Guergouz *et al.* (2018); (d) monazite U-Pb ages, after Henk *et al.* (1997).

mylonites, monazite grains show higher aspect ratios (highly elongated grains), and chemical zoning revealed more complex features with larger rims/tips over cores or and/or opposite chemical trends from core to rims with respect to monazite from protomylonites (Figure 5). These results are generally consistent with the microstructural results that show a higher degree of distortions strongly localized at the rims/tips of the monazite

grains from mylonites with respect to those from protomylonites (Figure 6).

7.b. Presence of three distinct monazite generations

Combining textural features with chemical data, X-ray maps and isotopic data, we recognized three generations of monazite. The main features of the three different generations are schematized in Figure 13a.

The first generation of monazite (MNZI) is defined by grains partially or totally included within garnet porphyroclasts (shielding effect) and domains of monazite occurring along the foliation. MNZI grains/domains are more abundant within protomylonites (Figure 7, 13a) and are associated with Carboniferous-Permian concordant dates (314–250 Ma). Monazite grains from mylonites partially enclosed within garnet were also able to locally preserve old dates but often discordant (e.g. Janots *et al.* 2008). The preservation of old dates within the foliation is a common feature of sheared rocks (e.g. Langone *et al.* 2011) and highlights the heterogeneous behaviour of monazite (or more generally of geochronometers) as a function of the hosting microdomain and shear partitioning. MNZI grains/domains are generally characterized by patchy zoning of both Th and Y and/or cores poorer in Y with respect to the rims/ external domains. The patchy zoning of both Th and Y is probably the result of an aggregation of small monazite grains in lower-amphibolite-facies rock, pseudomorph after (probable) allanite (e.g. Skrzypek *et al.* 2018; Williams *et al.* 2018). The low-Y cores of MNZI grains lying along the foliation or in contact with matrix-forming minerals (Figure 13a) formed likely during or after garnet growth that is able to fractionate Y as well as HREE (e.g. Rubatto *et al.* 2006; Taylor *et al.* 2014).

The second generation of monazite (MNZII) refers to rims/ domains with higher Y concentrations (MNZIIa, Figure 13a) with respect to cores or adjacent domains (i.e. MNZI). MNZIIa domains are characterized by lobate, inward-penetrating shapes with sharp contact with the inner domains suggesting the migration of a reaction front. These features have been suggested as criteria to identify the Coupled Dissolution-Precipitation process (CDP; Putnis *et al.* 2009; Harlov *et al.* 2011; Varga *et al.* 2020) and have been attributed to the inward progression of fluids/melts changing chemistry and/or isotopic record (Putnis *et al.* 2009; Weinberg *et al.* 2020; Varga *et al.* 2020). MNZIIa rims/domains are common within protomylonites but are more developed within mylonitic samples where they can be the 2/3 of the grain (Figure 5, 7, 13a). The isotopic data relative to the MNZIIa define a Triassic cluster of concordant dates (weighted average of 222 ± 8 Ma). The second generation of monazite is not only restricted to domains of replacement but also is seen as whole grains with elongated shapes (high aspect ratio) and high-Y content almost homogeneously distributed along the grain or with low-Y 'tips' (MNZIIb on Figure 13a). Monazite grains with these features were observed exclusively within mylonites and provided Triassic dates (weighted average of 238 ± 8 Ma; Figure 7, 13a). The internal, external and isotopic features suggest a syn-kinematic development of MNZIIb grains/domains whose ages are related to a specific tectonic event (e.g. Williams & Jercinovic, 2002). The observed textural and internal features suggest that the Y-rich MNZIIb grains are probably the result of a more pervasive CDP process that, as well as for MNZIIa, may reflect a period of monazite formation coevally with the breakdown of garnet (releasing Y). The higher proportion of MNZII over MNZI within mylonites is correlated with a more intense garnet break-down (Figure 13a) as documented by grain-

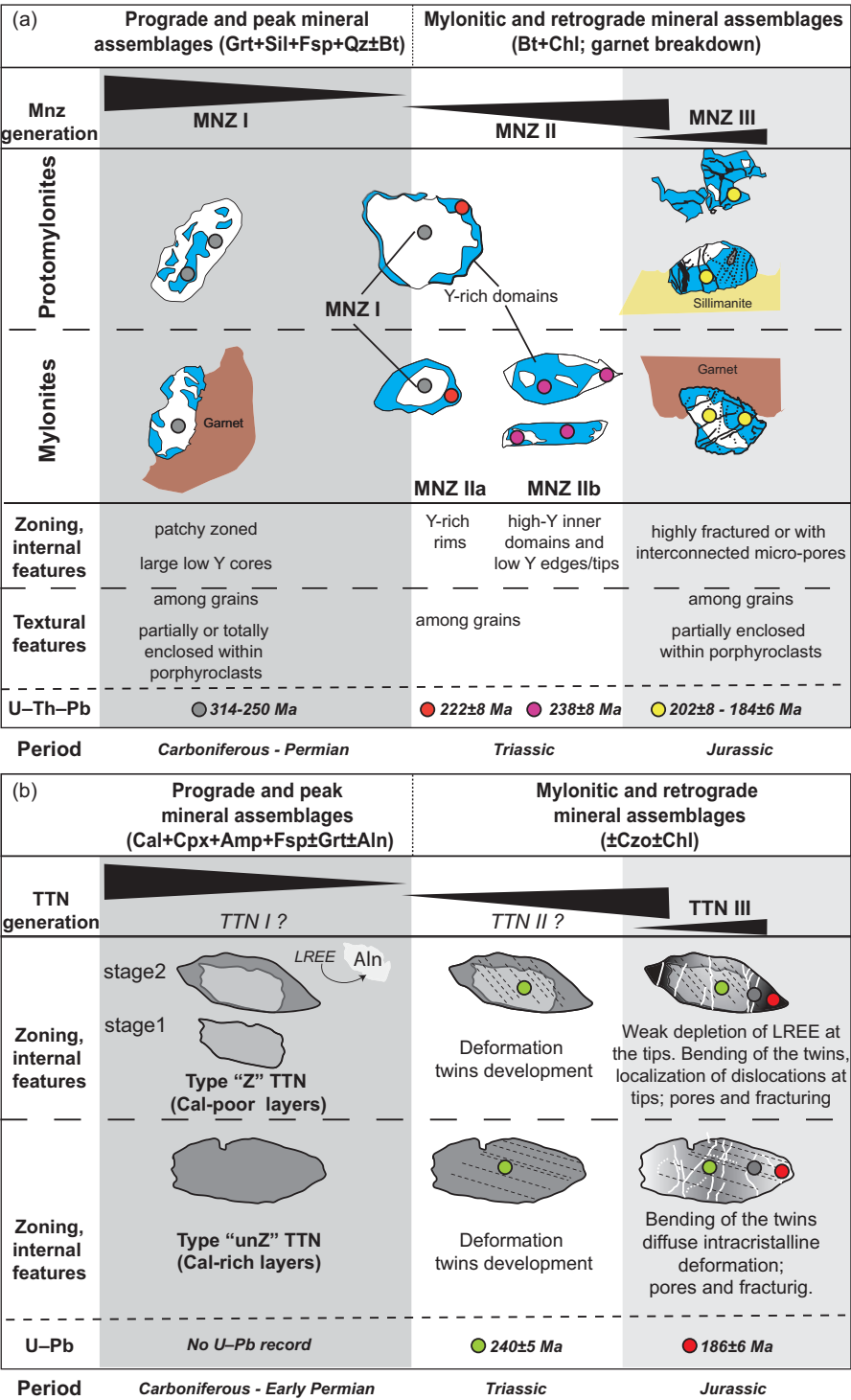


Figure 13. Synoptic summary of different generations of monazite (a) within protomylonitic and mylonitic paragneisses and titanite (b) within mylonitic calc-silicates. For each generation, the main microstructures, chemical zoning features and U-Pb data are reported as well as the main mineral assemblages.

size reduction and shaping of garnet becoming smaller, elliptic or rounded. The Y released during garnet break-down is thus incorporated within the external domains (MNZIIa) and/or grains (MNZIIb) of monazite formed by CDP.

The last generation of monazite (MNZIII) is defined by a few grains/domains providing mostly Jurassic concordant dates (nine data; dates ranging from 202±8 to 184±6 Ma; Figure 13a). MNZIII grains/domains were observed mainly within protomylonites (e.g. Mnz4a, VSDO-13B1; Mnz6c, VSDO-13A1; Mnz8c, VSDO-13A2; Figure 5 and Figure S1) and rarely within mylonites (Mnz9,

VSDO-13M1 in Figure S1; Figure 13a). MNZIII is mostly defined by small, isolated grains occurring as satellites around larger grains and by domains of grains characterized by (i) numerous fractures and/or (ii) anhedral shapes and/or (iii) numerous pores. The relatively large spread of dates and the presence of interconnected nano- and micro-porosity, as well as fractures, are markers that can indicate a late interaction with fluid (e.g. Harlov *et al.* 2011) and/or a partial replacement of monazite by a nanomixture of the different monazite generations (e.g. Grand’Homme *et al.* 2016; Hentschel *et al.* 2020).

The observed generations of monazite do not show well-defined age clusters being the concordant U–Th–Pb smeared from Carboniferous to Jurassic (Figure 7, 12a). This is more apparent for protomylonitic samples. In order to explain this continuous distribution of the concordant U–Th–Pb data, two possible phenomena can be argued: (i) the physical mixing of domains with different ages within the grain and/or (ii) the partial resetting of monazite during subsequent events. Weinberg *et al.* (2020) studied monazite in migmatites and suggested that the physical mixing had no influence on the age spread that was mainly controlled by the fact that the radiogenic Pb was not completely removed during the CDP reactions occurred during the younger events (Seydoux-Guillaume *et al.* 2003). Therefore, we here interpret the observed dates distribution within sheared rocks as reflecting inheritance from the regional HT metamorphism (MNZI), the development of syn-shearing domains/grains by CDP during Triassic (MNZII, $238 \pm 8 - 222 \pm 8$ Ma), the late alteration of monazite grains/domains (MNZIII) during Jurassic by interaction with fluids locally promoted by intracrystalline deformation.

7.c. Titanite heterogeneity controlled by the local environment

Two types of titanite were recognized within the calc-silicate sample: (i) titanite characterized by an apparent zoning, higher REE content and lying mostly within calcite-poor layers (type ‘Z’ titanite); (ii) homogeneous titanite with lower REE contents and occurring preferentially within calcite-rich layers (type ‘unZ’ titanite). The main features of the two titanite types are schematized in Figure 13b.

The occurrence of these two distinct types of titanite within the same thin-section suggests that the calc-silicate sample is made of different protoliths, i.e. siliciclastic/volcanoclastic and carbonate/marl (Figure 13b). The same observation has been recently made by Corvò *et al.* (2022, 2023) for titanite within mylonitic rocks from the Anzola Shear Zone from the adjacent Ossola valley (Figure 1a). In these rocks, the chemistry of titanite together with the mineral assemblages suggests the presence of alternating layers made of amphibolites and calc-silicates, i.e. former siliciclastic/volcanoclastic and carbonate/marl layers, respectively.

The local environment exerted a fundamental role also on the deformation features recorded by titanite (Figure 13b). While deformation twinning is common for both ‘Z’ and ‘unZ’ types, titanite grains from calcite-poor portions (type ‘Z’) show higher lattice distortions (up to 21°) focused on rims/tips with respect to ‘unZ’ titanite from calcite-rich portions. A similar correlation between microstructure and the composition of the microdomain hosting titanite has been described for the banded (amphibolites – calc-silicates) mylonites of the Anzola Shear Zone exposed in the adjacent Ossola valley (Figure 1a; Corvò *et al.* 2023).

7.d. Petrogenesis of titanite vs U–Pb record: a decoupling between chemistry and isotopes

Figure 13b summarizes the suggested petrogenetic evolution of titanite as well as the observed microstructures and the isotopic record. Titanite is occurring within the matrix and is also included within clinopyroxene porphyroclasts (Figure 8h). In both cases, it shows the same zoning and chemical features. These observations suggest that titanite formed at least coevally with the peak metamorphic assemblage during the Permian high-temperature regional metamorphism. Since the occurrence of sphene in metamorphic rocks is strongly controlled by bulk composition

(Frost *et al.* 2001), the composite nature of our sample, i.e. former siliciclastic/volcanoclastic and carbonate/marl layers, would imply different metamorphic reactions for the formation of titanite. According to the phase relations diagram for calcite-bearing rocks, titanite could be produced and stable at high temperatures and $X(\text{H}_2\text{O})$ conditions during regional metamorphism by reactions involving calcite, quartz and rutile \pm clino/zoisite (e.g. Frost *et al.* 2001; Kohn, 2017). Within the silicate-rich layers, the formation of titanite during metamorphism needs further reactants such as chlorite, clinopyroxene, amphibole, plagioclase and ilmenite (e.g. Frost *et al.* 2001; Kohn, 2017). The reactions involving the above-mentioned reactants may explain the formation of titanite observed within both calcite-poor and calcite-rich domains of the studied sample during the HT regional metamorphism. The apparent zoning consisting of a depletion of LREE, Y and Zr in the external portions of type ‘Z’ titanite can be explained by two alternative processes. This feature is compatible with the occurrence of large allanite (LREE-rich epidote) grains grown almost coevally with titanite within the silicate-rich layers (Figure 3g). Alternatively, the LREE depletion of the external domains for titanite could be related by the occurrence of clinozoisite developed during deformation (Figure 3h). The lack of an apparent zoning within type ‘unZ’ titanite and the occurrence of clinozoisite within both layers suggest that the observed zoning is a primary feature due to the formation of allanite almost coevally with titanite (stage 2 on Figure 13b).

The pre-shear mineral assemblages of both calcite-poor and calcite-rich layers contain garnet. The observed REE pattern for titanite may be useful to unravel the genetic relationships between garnet and titanite. The lack of a significant and general HREE fractionation for the analysed titanite grains (Figure 9c,d) indicates that titanite probably predates garnet formation. Alternatively, the possible HREE fractionation exerted by garnet coeval or predating titanite is extremely local (e.g. Ttn23, Figure 9d). According to the P–T–X(CO_2) modelling of Rapa *et al.* (2017) for both calcite-poor and calcite-rich domains of calc-silicates from Himalaya, different episodes of titanite growth are predicted before the formation of garnet-bearing assemblages. These observations are more compatible with our first hypothesis of a garnet postdating titanite. Summarizing, the observed titanite grains are the result of different metamorphic reactions, as a function of the hosting microdomains, producing allanite almost coevally with titanite (stage 2 on Figure 13b) and predating garnet during regional HT metamorphism. This petrogenetic reconstruction is coherent with the Zr-in-titanite temperature estimates obtained for the internal domains of titanite indicating high-temperature conditions ($919 \pm 82 - 746 \pm 50^\circ\text{C}$). These temperatures overlap, or are even higher than, the peak temperatures estimated from the adjacent mafic and pelitic metamorphic rocks (Figure 9; Kunz & White, 2019). Even though the titanite rims provided lower temperature with respect to the cores ($850 \pm 57 - 741 \pm 49^\circ\text{C}$), these remain still significantly higher with respect to the qualitative (syn-kinematic mineral assemblages suggest epidote-bearing amphibolite-facies conditions) and quantitative estimates of temperature conditions of deformation ($<700^\circ\text{C}$; Simonetti *et al.* 2023).

Contrarily to monazite showing three distinct generations it has not been possible to define different generations for titanite combining U–Pb isotopes with chemistry and microstructures (Figure 13b). The U–Pb data obtained from titanite are bounded by two regression lines with lower intercept ages at 240 ± 5 and 186 ± 6 Ma (Figure 11, 13b). These two regression lines are correlated with textural position being the oldest related to the cores and the

youngest linked to the rims/tips of titanite. The time interval framed by the two regression lines does not fit with (postdate) the main peaks of the Permian regional high-temperature metamorphism that has been constrained, in extreme detail, with zircon (Ewing *et al.* 2013; Kunz *et al.* 2018), monazite (Williams *et al.* 2022; Wyatt *et al.* 2022) and garnet (Connop *et al.* 2024; Bartoli *et al.* 2024) along the same crustal section (Figure 12b).

The oldest possible intercept age from the innermost portion of titanite grains points to Triassic (TTNII? in Figure 13b) indicating that this accessory mineral was not able to clearly retain the age of crystallisation (TTNI? in Figure 13b). The Triassic lower intercept age obtained from the innermost titanite domains could thus reflect: (i) the crystallization/cooling age or (ii) a total reset of the isotopic system within a pre-existing grain. As discussed above, titanite formed during the Permian regional metamorphism, coevally with the first generation of monazite (MNZI in Figure 13a), therefore, the first hypothesis is unlikely. The studied crustal levels experienced high-temperature conditions for a long-time interval causing a spread of the zircon (Ewing *et al.* 2013; Kunz *et al.* 2018) and monazite ages (Williams *et al.* 2022; Wyatt *et al.* 2022). At these temperatures, the U–Pb system of zircon and monazite was partially reset, whereas within titanite, it was completely open until the Triassic. Alternatively, a Triassic event caused a total reset of the titanite U–Pb record. The U–Pb data distribution strongly correlated with the position within the grain of titanite could reflect a volume diffusion process enhanced by deformation twins (e.g. Bonamici *et al.* 2015; Moser *et al.* 2022; Corvò *et al.* 2023; Kavanagh-Lepage *et al.* 2023) that are common features of both titanite types (Figure 13b). At the high-temperature stage of shearing, the development of deformation twins promoted the evacuation of the radiogenic ions (e.g. Kavanagh-Lepage *et al.* 2023). The oldest lower intercept age obtained from the inner portions of titanite is partially overlapping the age of syn-kinematic monazite (i.e. MNZII: 222 ± 8 and 238 ± 8 Ma). This observation supports the alternative interpretation of the old lower intercept age marks the beginning of deformation. The U–Pb lower intercept age obtained from the external domains (rims/tips) partially showing evidence for intracrystalline deformation (localized higher dislocation density) of both titanite types (TTNIII in Figure 13b) may thus reflect the end of volume diffusive loss of Pb and a localized deformation-induced isotopic reset (Stearns *et al.* 2015; Moser *et al.* 2022). Recently, Corvò *et al.* (2023) reported the same interpretation for titanite grains within the Anzola Shear Zone, which can be considered as the NE prolongation of the shear zone studied in this work.

In summary, titanite preserved the internal features (chemistry and zoning) from the Permian regional metamorphic event while the U–Pb data have no memory of it, recording mostly the deformation-induced resetting and volume diffusion. Several authors have recently described similar features studying titanite in sheared rocks (Kavanagh-Lepage *et al.* 2023; Corvò *et al.* 2023): deformation influenced the U–Pb system without promoting significant modification of titanite chemistry (geochemical decoupling).

7.e. Complementary behaviour of monazite and titanite

Combining the chemical, isotopic and microstructural features, we recognized a contrasting behaviour of monazite and titanite that likely provided complementary information (Figure 11–13). The former experienced an intense reactivity (CDP) during Triassic with the involvement of garnet (e.g. Y-enriched rims/domains/

grains; MNZII on Figure 13a). Locally, it developed internal features (chemistry, fractures and pores) suggesting a fluid-assisted phase of isotopic perturbation during Jurassic (MNZIII on Figure 13a). Monazite was also able to substantially preserve the age information relative to the prograde HT metamorphism, resulting thus partially resilient to the subsequent deformation events (MNZI on Figure 13a).

Titanite on the contrary was almost chemically unreactive during deformation preserving the zoning features developed during the prograde metamorphism (chemical resiliency). On the other hand, titanite has not retained the age of the Permian HT metamorphism (TTNI? on Figure 13b), as documented by monazite in this work and from literature (Bartoli *et al.* 2024; Connop *et al.* 2024; Wyatt *et al.* 2022; Williams *et al.* 2022; Henk *et al.* 1997). A similar decoupling between chemistry and U–Pb isotopic data has been already described for titanite in amphibolite and calc-silicate (Holder & Hacker, 2019; Kavanagh-Lepage *et al.* 2023; Corvò *et al.* 2023). Titanite demonstrated a more pronounced intracrystalline deformation, with respect to monazite, as documented by deformation twins across the grains and the localization of dislocations at rims/tips. These features could be responsible for the observed decoupling, allowing more efficiently the mobility of U and Pb isotopes (along the dislocation boundaries, e.g. Bonamici *et al.* 2015) with respect to the other trace elements. Moreover, in the presence of abundant silicates surrounding titanite, the deformation at the rim/tips is generally more intense, and thus, the U–Pb data of these domains might reflect both volume diffusion and recrystallization.

Combining the complementary information from the two investigated geochronometers and thanks to their different behaviour during shearing, it has been possible to reconstruct the timing of the shear zone activity otherwise only partially recorded.

7.f. Regional implications: rift-related shear zone activity from Middle Triassic (Ladinian) to Early Jurassic (Sinemurian)

The Forno-Rosarolo shear zone developed within metasedimentary rocks characterized by metamorphic conditions at the transition between granulite and amphibolite facies (Redler *et al.* 2012; Kunz *et al.* 2014; Kunz & White, 2019; Simonetti *et al.* 2023). Deformation overprinted mainly paragneisses and metabasites, which experienced extensive partial melting during Permian time. Petrographic and microstructural observations on mylonitic paragneisses suggest that deformation developed under amphibolite-facies conditions ($\sim 650^\circ\text{C}$ and $\sim 0.55\text{GPa}$; Simonetti *et al.* 2023). The rare occurrence of chlorite at the expense of biotite and the sillimanite replacement by white mica indicate that mylonites were poorly affected by green-schist retrograde overprint (Simonetti *et al.* 2023).

Integrating the U–Th–Pb data with textural, microstructural and chemical features of monazite, the activity of the shear zone can be constrained from two monazite generations. The main one, MNZII, documents the amphibolite-facies ductile shearing with the formation of tiny, syn-kinematic Y-rich monazite grains (238 ± 8 Ma) and Y-rich rims (222 ± 8 Ma) around old cores (MNZI: $314\text{--}250$ Ma). This Triassic event represents the beginning of a syn-rift deformation that has been recorded at different crustal levels within the IVZ (e.g. Langone *et al.* 2018). During the late stage of the amphibolite-facies deformation, the interplay between deformation and fluids promoted the formation of the third generation of monazite (MNZIII; from 202 ± 8 to 184 ± 6 Ma) within

sheared paragneisses and the formation of the rims/tips of titanite within the mylonitic calc-silicates (TTNIII; lower intercept age at 186 ± 6 Ma). Both the last generation of monazite and the rim/tips of titanite can be attributed to the end of deformation under amphibolite-facies condition across the Triassic-Jurassic boundary. It is interesting to note that recently a similar conclusion has been suggested by Corvò *et al.* (2023) for the Anzola Shear Zone from the adjacent Ossola valley, i.e. a northeast prolongation of the studied shear zone.

8. Conclusions

The activity of the shear zone has been constrained at the Triassic-Jurassic time by combining geochemical and U-(Th)-Pb data from monazite and titanite within sheared migmatitic paragneisses and calc-silicates, respectively.

Monazite chemical and isotopic signature is directly affected by its deformation history. In protomylonitic paragneisses, monazite preferentially retained ages related to the regional HT metamorphism (resiliency), whereas in mylonites monazite was more able to record the deformation events (reactivity). The Y-rich syn-kinematic domains/grains of monazite formed during the Triassic ($238 \pm 8 - 222 \pm 8$ Ma) due to a CDP process coevally with the breakdown of garnet (releasing Y).

On the contrary, although titanite was almost chemically unreactive during deformation (resiliency), its U-Pb isotopic system was not able to retain the Permian regional metamorphism. The U-Pb data are correlated with textural and microstructural features. The titanite innermost domains provide a Triassic lower intercept age (240 ± 5 Ma) indicating a total isotopic reset at the beginning of deformation. This was favoured by the occurrence of deformation twins across the titanite grains acting as preferential pathways for the U and Pb isotopes. The rims/tips of titanite, partially overlapping the zone of accumulation of dislocations, define a Jurassic lower intercept age at 186 ± 6 Ma. The entire U-Pb dataset is, thus, reflecting the combined effect of a deformation-induced volume diffusion and recrystallization.

The reconstructed timing of deformation suggests a strong causal relationship to the Triassic-Jurassic rifting event leading to the opening of the Alpine Tethys that affected the Adria continental crust. Hence, mid-crustal shear zones such as the one studied played a fundamental role in accommodating deformation.

Our study shows that combining age information from different geochronometers within different protoliths and/or showing different fabrics (i.e. protomylonitic and mylonitic) allows to unveil the details of shear zone activity.

Supplementary material. The supplementary material for this article can be found at <https://doi.org/10.1017/S0016756825100022>

Acknowledgements. The following projects partially funded this research: PRIN2017 'Micro to Macro - how to unravel the nature of the large magmatic events' (20178LPCPW- Langone Antonio); Fondazione Cariplo, project 'MADAM', grant n° 2024-0348 (Stefania Corvò).

References

Austrheim H (2013) Fluid and deformation induced metamorphic processes around Moho beneath continent collision zones: Examples from the exposed root zone of the Caledonian mountain belt, W-Norway. *Tectonophysics* **609**, 620–35.

- Bartoli O, Millonig LJ, Carvalho BB, Marschall HR and Gerdes A** (2024) The age of granulite-facies metamorphism in the Ivrea-Verbano Zone (NW Italy) determined through in situ U-Pb dating of garnet. *Journal of Petrology* **65**, egae083. <https://doi.org/10.1093/petrology/egae083>
- Beach A** (1976) The interrelations of fluid transport, deformation, geochemistry and heat flow in early Proterozoic shear zones in the Lewisian complex. *Philosophical Transactions for the Royal Society of London Series A, Mathematical and Physical Sciences* **280**, 569–604.
- Beltrando M, Stockli DF, Decarlis A and Manatschal G** (2015) A crustal-scale view at rift localization along the fossil Adriatic margin of the Alpine Tethys preserved in NW Italy. *Tectonics* **34**, 1927–51. <https://doi.org/10.1002/2015TC003973>
- Bergemann CA, Gnos E, Berger A, Janots E and Whitehouse MJ** (2020) Dating tectonic activity in the Lepontine Dome and Rhone-Simplon Fault regions through hydrothermal monazite-(Ce). *Solid Earth* **11**, 199–222. <https://doi.org/10.5194/se-11-199-2020>
- Bertolani M** (1968) Sguardo generale alla petrografia della Valle S trona (Novara). Guida all'escursione. *Schweizerische Miner, Petr, Mitt* **48**, 314–28.
- Bonamici CE, Fanning CM, Kozdon R, Fournelle JH and Valley JW** (2015) Combined oxygen-isotope and U-Pb zoning studies of titanite: New criteria for age preservation. *Chemical Geology* **398**, 70–84. <https://doi.org/10.1016/j.chemgeo.2015.02.002>
- Boriani A, Burlini L and Sacchi R** (1990) The Cossato-Mergozzo-Brissago Line and the Pogallo Line (Southern Alps, Northern Italy) and their relationships with the late-Hercynian magmatic and metamorphic events. *Tectonophysics* **182**, 91–102. [https://doi.org/10.1016/0040-1951\(90\)90344-8](https://doi.org/10.1016/0040-1951(90)90344-8)
- Boriani AC and Villa IM** (1997) Geochronology of regional metamorphism in the Ivrea-Verbano Zone and Serie dei Laghi, Italian Alps. *Schweizerische Mineralogische und Petrographische Mitteilungen* **77**, 381–401. <https://doi.org/10.5169/SEALS-58492>
- Bosse V and Villa IM** (2019) Petrochronology and hygrochronology of tectono-metamorphic events. *Gondwana Research* **71**, 76–90.
- Brodie KH** (1981) Variation in amphibole and plagioclase composition with deformation. *Tectonophysics* **78**, 385–402. [https://doi.org/10.1016/0040-1951\(81\)90021-4](https://doi.org/10.1016/0040-1951(81)90021-4)
- Brodie KH and Rutter EH** (1987) Deep crustal extensional faulting in the Ivrea Zone of Northern Italy. *Tectonophysics* **140**, 193–212. [https://doi.org/10.1016/0040-1951\(87\)90229-0](https://doi.org/10.1016/0040-1951(87)90229-0)
- Brodie KH, Rutter EH and Rex D** (1989) On the age of deep crustal extensional faulting in the Ivrea zone, northern Italy. *Geological Society, London, Special Publications* **45**, 203–10. <https://doi.org/10.1144/GSL.SP.1989.045.01.11>
- Carosi R, Montomoli C, Iaccarino S, Benetti B, Petrocchia A and Simonetti M** (2022) Constraining the timing of evolution of shear zones in two collisional orogens: Fusing structural geology and geochronology. *Geosciences* **12**, 231. <https://doi.org/10.3390/geosciences12060231>
- Carvalho BB, Bartoli O, Ferri F, Cesare B, Ferrero S, Remusat L, Capizzi LS and Poli S** (2019) Anatexis and fluid regime of the deep continental crust: New clues from melt and fluid inclusions in metapelitic migmatites from Ivrea Zone (NW Italy). *Journal of Metamorphic Geology* **37**, 951–75. <https://doi.org/10.1111/jmg.12463>
- Cherniak DJ** (1993) Lead diffusion in titanite and preliminary results on the effects of radiation damage on Pb transport. *Chemical Geology* **110**, 177–94. [https://doi.org/10.1016/0009-2541\(93\)90253-F](https://doi.org/10.1016/0009-2541(93)90253-F)
- Connop CH, Smye AJ, Garber JM, Moser AC, Caddick MJ and Vervoort JD** (2024) Assembly of lower continental crust: A garnet Lu-Hf petrochronological investigation of the Ivrea-Verbano Zone, Italy. *Earth and Planetary Science Letters* **634**, 118677. <https://doi.org/10.1016/j.epsl.2024.118677>
- Corvò S, Kylander-Clark AR and Langone A** (2024) Titanite petrochronological data across the continental crust section exposed in Val d'Ossola (Ivrea-Verbano Zone, Italy). *Data in Brief* **56**, 110804. <https://doi.org/10.1016/j.dib.2024.110804>
- Corvò S, Langone A, Padrón-Navarta JA, Tommasi A and Zanetti A** (2020) Porphyroclasts: Source and sink of major and trace elements during deformation-induced metasomatism (Finero, Ivrea-Verbano Zone, Italy). *Geosciences* **10**, 196. <https://doi.org/10.3390/geosciences10050196>
- Corvò S, Maino M, Piazzolo S, Kylander-Clark ARC, Seno S and Langone A** (2023) Crystal plasticity and fluid availability govern the ability of titanite to

- record the age of deformation. *Earth and Planetary Science Letters* **620**, 118349. <https://doi.org/10.1016/j.epsl.2023.118349>
- Corvò S, Maino M, Piazzolo S, Seno S and Langone A (2022) Role of inherited compositional and structural heterogeneity in shear zone development at mid-low levels of the continental crust (the Anzola shear zone; Ivrea-Verbano Zone, Southern Alps). *Lithos* **422–423**, 106745. <https://doi.org/10.1016/j.lithos.2022.106745>
- Corvò S., Montemagni C, Zanchetta S and Langone A (2025) Intermittent brittle and ductile deformation as recorded by dating of ultramylonites and pseudotachylytes in extending continental crust (Ivrea-Verbano Zone, Italy). *Terra Nova*, <https://doi.org/10.1111/ter.12775>
- Cruz MJ, Cunha JC, Merlet C and Sabaté P (1996) Datação punctual das monazitas da região de Itambé, Bahia, através da microsonda eletrônica. XXXIX Congresso Brasileiro de Geologia vol. 2 Sociedade Brasileira de Geologia-Núcleo, Bahia-Segipe, pp. 206–209.
- Cruz-Urbe AM, Feineman MD, Zack T and Barth M (2014) Metamorphic reaction rates at ~650–800°C from diffusion of niobium in rutile. *Geochim Cosmochim Acta* **130**, 63–77. <https://doi.org/10.1016/j.gca.2013.12.015>
- Degli Alessandrini G (2018) Deformation mechanisms and strain localization in the mafic continental lower crust. School of Geography, Earth and Environmental Science. University of Plymouth, Plymouth. Published thesis.
- Di Vincenzo G, Carosi R, Palmeri R and Tiepolo M (2007) A comparative U–Th–Pb (zircon–monazite) and 40Ar–39Ar (muscovite–biotite) study of shear zones in northern Victoria Land (Antarctica): Implications for geochronology and localized reworking of the Ross Orogen. *Journal of Metamorphic Geology* **25**, 605–30. <https://doi.org/10.1111/j.1525-1314.2007.00717.x>
- Didier A, Bosse V, Cherneva Z, Gautier P, Georgieva M, Paquette JL and Gerdjikov I (2014) Syn-deformation fluid-assisted growth of monazite during renewed high-grade metamorphism in metapelites of the Central Rhodope (Bulgaria, Greece). *Chemical Geology* **381**, 206–22.
- Engi M (2017) Petrochronology based on REE-minerals: Monazite, allanite, xenotime, apatite. *Reviews in Mineralogy and Geochemistry* **83**, 365–418. <https://doi.org/10.2138/rmg.2017.83.12>
- Erickson TM, Pearce MA, Taylor RJM, Timms NE, Clark C, Reddy SM and Buick IS (2015) Deformed monazite yields high-temperature tectonic ages. *Geology* **43**, 383–6. <https://doi.org/10.1130/G36533.1>
- Ewing TA, Hermann J and Rubatto D (2013) The robustness of the Zr-in-rutile and Ti-in-zircon thermometers during high-temperature metamorphism (Ivrea-Verbano Zone, northern Italy). *Contributions to Mineralogy and Petrology* **165**, 757–79. <https://doi.org/10.1007/s00410-012-0834-5>
- Ewing TA, Rubatto D, Beltrando M and Hermann J (2015) Constraints on the thermal evolution of the Adriatic margin during Jurassic continental break-up: U–Pb dating of rutile from the Ivrea–Verbano Zone, Italy. *Contributions to Mineralogy and Petrology* **169**, 44. <https://doi.org/10.1007/s00410-015-1135-6>
- Förster H-J (1998) The chemical composition of REE–Y–Th–U-rich accessory minerals in peraluminous granites of the Erzgebirge-Fichtelgebirge region, Germany; Part I, The monazite-(Ce)-brabantite solid solution series. *American Mineralogist* **83**, 259–72. <https://doi.org/10.2138/am-1998-3-409>
- Frost BR, Chamberlain KR and Schumacher JC (2001) Sphene (Titanite): Phase relations and role as a geochronometer. *Chemical Geology* **172**, 131–48. [https://doi.org/10.1016/S0009-2541\(00\)00240-0](https://doi.org/10.1016/S0009-2541(00)00240-0)
- Garde AA, Boriani A and Sørensen EV (2015) Crustal modelling of the Ivrea–Verbano zone in northern Italy re-examined: Coseismic cataclasis versus extensional shear zones and sideways rotation. *Tectonophysics* **662**, 291–311. <https://doi.org/10.1016/j.tecto.2015.04.003>
- Gordon SM, Kirkland CL, Reddy SM, Blatchford HJ, Whitney DL, Teyssier C, Evans NJ and McDonald BJ (2021) Deformation-enhanced recrystallization of titanite drives decoupling between U–Pb and trace elements. *Earth and Planetary Science Letters* **560**, 116810. <https://doi.org/10.1016/j.epsl.2021.116810>
- Grand'homme A, Janots E, Seydoux-Guillaume A-M, Guillaume D, Bosse V and Magnin V (2016) Partial resetting of the U–Th–Pb systems in experimentally altered monazite: Nanoscale evidence of incomplete replacement. *Geology* **44**, 431–4. G37770.1.
- Guergouz C, Martin L, Vanderhaeghe O, Thébaud N and Fiorentini M (2018) Zircon and monazite petrochronologic record of prolonged amphibolite to granulite facies metamorphism in the Ivrea-Verbano and Strona-Ceneri Zones, NW Italy. *Lithos* **308–309**, 1–18. <https://doi.org/10.1016/j.lithos.2018.02.014>
- Harlov DE, Wirth R and Hetherington CJ (2011) Fluid-mediated partial alteration in monazite: The role of coupled dissolution–reprecipitation in element redistribution and mass transfer. *Contributions to Mineralogy and Petrology* **162**, 329–48. <https://doi.org/10.1007/s00410-010-0599-7>
- Hartnady MIH, Kirkland CL, Clark C, Spaggiari CV, Smithies RH, Evans NJ and McDonald BJ (2019) Titanite dates crystallization: Slow Pb diffusion during super-solidus re-equilibration. *Journal of Metamorphic Geology* **37**, 823–38. <https://doi.org/10.1111/jmg.12489>
- Hayden LA, Watson EB and Wark DA (2008) A thermobarometer for sphene (titanite). *Contributions to Mineralogy and Petrology* **155**, 529–40. <https://doi.org/10.1007/s00410-007-0256-y>
- Henk A, Franz L, Teufel S and Oncken O (1997) Magmatic underplating, extension, and crustal reequilibration: Insights from a cross-section through the Ivrea Zone and Strona-Ceneri Zone, Northern Italy. *The Journal of Geology* **105**, 367–78. <https://doi.org/10.1086/515932>
- Hentschel F, Janots E, Treppmann CA, Magnin V and Lanari P (2020) Corona formation around monazite and xenotime during greenschist-facies metamorphism and deformation. *European Journal of Mineralogy* **32**, 521–44.
- Hetherington CJ, Backus EL, McFarlane CRM, Fisher CM and Pearson DG (2017) Origins of Textural, compositional, and isotopic complexity in monazite and its petrochronological analysis. In *Microstructural Geochronology Planetary Records Down to Atom Scale* (eds DE Moser, F Corfu, JR Darling, SM Reddy and K Tait), pp. 63–90. Geophysical Monograph Series, John Wiley & Sons, Inc. <https://doi.org/10.1002/9781119227250.ch3>
- Hodges KV and Fountain DM (1984) Pogallo Line, South Alps, northern Italy: An intermediate crustal level, low-angle normal fault? *Geology* **12**, 151–5.
- Holder RM and Hacker BR (2019) Fluid-driven resetting of titanite following ultrahigh-temperature metamorphism in southern Madagascar. *Chemical Geology* **504**, 38–52. <https://doi.org/10.1016/j.chemgeo.2018.11.017>
- Holder RM, Hacker BR, Seward GGE and Kylander-Clark ARC (2019) Interpreting titanite U–Pb dates and Zr thermobarometry in high-grade rocks: Empirical constraints on elemental diffusivities of Pb, Al, Fe, Zr, Nb, and Ce. *Contributions to Mineralogy and Petrology* **174**, 42. <https://doi.org/10.1007/s00410-019-1578-2>
- Janots E, Berger A, Gnos E, Whitehouse M, Lewin E and Peqke T (2012) Constraints on fluid evolution during metamorphism from U–Th–Pb systematics in Alpine hydrothermal monazite. *Chemical Geology* **326–327**, 61–71.
- Janots E, Engi M, Berger A, Allaz J, Schwarz J-O and Spandler C (2008) Prograde metamorphic sequence of REE minerals in pelitic rocks of the Central Alps: Implications for allanite–monazite–xenotime phase relations from 250 to 610 degrees C. *Journal of Metamorphic Geology* **26**, 509–26.
- Karakas O, Wotzlav JF, Guillong M, Ulmer P, Brack P, Economos R, Bergantz GW, Sinigoi S and Bachmann O (2019) The pace of crustal-scale magma accretion and differentiation beneath silicic caldera volcanoes. *Geology* **47**, 719–23.
- Kavanagh-Lepage C, Gervais F, Larson K, Graziani R and Moukhsil A (2023) Deformation induced decoupling between U–Pb and trace elements in titanite revealed through petrochronology and study of localized deformation. *Geoscience Frontiers* **14**, 101496. <https://doi.org/10.1016/j.gsf.2022.101496>
- Kenkmann T (2000) Processes controlling the shrinkage of porphyroclasts in gabbroic shear zones. *Journal of Structural Geology* **22**, 471–87. [https://doi.org/10.1016/S0191-8141\(99\)00177-7](https://doi.org/10.1016/S0191-8141(99)00177-7)
- Kenkmann T and Dresen G (2002) Dislocation microstructure and phase distribution in a lower crustal shear zone – an example from the Ivrea-Zone, Italy. *International Journal of Earth Sciences* **91**, 445–58. <https://doi.org/10.1007/s00531-001-0236-9>
- Kirkland CL, Olierook HKH, Danišik M, Liebmann J, Hollis J, Ribeiro BV and Rankenburg K (2023) Dating mylonitic overprinting of ancient rocks. *Communications Earth & Environment* **4**, 47. <https://doi.org/10.1038/s43247-023-00709-5>
- Kirkland CL, Yakymchuk C, Gardiner NJ, Szilas K, Hollis J, Olierook H and Steenfelt A (2020) Titanite petrochronology linked to phase equilibrium

- modelling constrains tectono-thermal events in the Akia Terrane, West Greenland. *Chemical Geology* **536**, 119467.
- Klemme S, Prowatke S, Münker C, Magee CW, Lahaye Y, Zack T, Kasemann SA, Cabato EJA and Kaeser B (2008) Synthesis and preliminary characterisation of new silicate, phosphate and titanite reference glasses. *Geostandards and Geoanalytical Research* **32**, 39–54.
- Klötzli US, Sinigoi S, Quick JE, Demarchi G, Tassinari CC, Sato K and Günes Z (2014) Duration of igneous activity in the Sesia Magmatic System and implications for high-temperature metamorphism in the Ivrea–Verbano deep crust. *Lithos* **206**, 19–33.
- Kohn MJ (2016) Metamorphic chronology—a tool for all ages: Past achievements and future prospects. *American Mineralogist* **101**, 25–42. <https://doi.org/10.2138/am-2016-5146>
- Kohn MJ (2017) Titanite petrochronology. *Reviews in Mineralogy and Geochemistry* **83**, 419–41. <https://doi.org/10.2138/rmg.2017.83.13>
- Kohn MJ, Engi M, Lanari P and Swainson I (eds) (2017) *Petrochronology: Methods and Applications*. Chantilly, VA: The Mineralogical Society of America.
- Kunz BE, Johnson TE, White RW and Redler C (2014) Partial melting of metabasic rocks in Val Strona di Omegna, Ivrea Zone, northern Italy. *Lithos* **190–191**, 1–12. <https://doi.org/10.1016/j.lithos.2013.11.015>
- Kunz BE, Regis D and Engi M (2018) Zircon ages in granulite facies rocks: Decoupling from geochemistry above 850°C? *Contributions to Mineralogy and Petrology* **173**, 26. <https://doi.org/10.1007/s00410-018-1454-5>
- Kunz BE and White RW (2019) Phase equilibrium modelling of the amphibolite to granulite facies transition in metabasic rocks (Ivrea Zone, NW Italy). *Journal of Metamorphic Geology* **37**, 935–50. <https://doi.org/10.1111/jmg.12478>
- Langone A, Braga R, Massonne H-J and Tiepolo M (2011) Preservation of old (prograde metamorphic) U–Th–Pb ages in unshielded monazite from the high-pressure paragneisses of the Variscan Ulten Zone (Italy). *Lithos* **127**, 68–85. <https://doi.org/10.1016/j.lithos.2011.08.007>
- Langone A, Zanetti A, Daczko NR, Piazzolo S, Tiepolo M and Mazzucchelli M (2018) Zircon U–Pb dating of a lower crustal shear zone: A case study from the northern sector of the Ivrea–Verbano Zone (Val Cannobina, Italy). *Tectonics* **37**, 322–42. <https://doi.org/10.1002/2017TC004638>
- Linthout K (2007) Tripartite division of the system 2REEPO₄–CaTh(po₄)₂ – 2ThSiO₄, discreditation of brabantite, and recognition of cheralite as the name for members dominated by CaTh(PO₄)₂. *The Canadian Mineralogist* **45**, 503–8. <https://doi.org/10.2113/gscanmin.45.3.503>
- Manatschal G, Müntener O, Lavier LL, Minshull TA and Péron-Pinvidic G (2007) Observations from the Alpine Tethys and Iberia–Newfoundland margins pertinent to the interpretation of continental breakup. *Geological Society, London, Special Publications* **282**, 291–324. <https://doi.org/10.1144/SP282.14>
- McDonough WF and Sun SS (1995) The composition of the Earth. *Chemical Geology* **120**, 223–53.
- Mcgregor M, Erickson TM, Spray JG and Whitehouse MJ (2021) High-resolution EBSD and SIMS U–Pb geochronology of zircon, titanite, and apatite: Insights from the Lac La Moine impact structure, Canada. *Contributions to Mineralogy and Petrology* **176**, 76. <https://doi.org/10.1007/s00410-021-01828-y>
- Mohn G, Manatschal G, Beltrando M, Masini E and Kuszniir N (2012) Necking of continental crust in magma-poor rifted margins: Evidence from the fossil Alpine Tethys margins: Necking of continental crust. *Tectonics* **31**. <https://doi.org/10.1029/2011TC002961>
- Moser AC, Hacker BR, Gehrels GE, Seward GGE, Kylander-Clark ARC and Garber JM (2022) Linking titanite U–Pb dates to coupled deformation and dissolution–reprecipitation. *Contributions to Mineralogy and Petrology* **177**, 42. <https://doi.org/10.1007/s00410-022-01906-9>
- Mottram CM and Cottle JM (2024) An electron backscatter diffraction study of monazite: Linking the time-deformation path. *Chemical Geology* **663**, 122238.
- Mulch A, Cosca M and Handy M (2002) In-situ UV-laser ⁴⁰Ar/³⁹Ar geochronology of a micaceous mylonite: An example of defect-enhanced argon loss. *Contributions to Mineralogy and Petrology* **142**, 738–52. <https://doi.org/10.1007/s00410-001-0325-6>
- Oberti R, Smith DC, Rossi G and Caucia F (1981) The crystal-chemistry of high-aluminium titanites. *European Journal of Mineralogy* **3**, 777–92.
- Olierook HKH, Taylor RJM, Erickson TM, Clark C, Reddy SM, Kirkland CL, Jahn I and Barham M (2019) Unravelling complex geologic histories using U–Pb and trace element systematics of titanite. *Chemical Geology* **504**, 105–22. <https://doi.org/10.1016/j.chemgeo.2018.11.004>
- Oriolo S, Wemmer K, Oyhantçabal P, Fossen H, Schulz B and Siegesmund S (2018) Geochronology of shear zones – a review. *Earth-Science Reviews* **185**, 665–83. <https://doi.org/10.1016/j.earscirev.2018.07.007>
- Papapavlou K, Darling JR, Storey CD, Lightfoot PC, Moser DE and Lasalle S (2017) Dating shear zones with plastically deformed titanite: New insights into the orogenic evolution of the Sudbury impact structure (Ontario, Canada). *Precambrian Research* **291**, 220–35. <https://doi.org/10.1016/j.precamres.2017.01.007>
- Parrish RR (1990) U–Pb dating of monazite and its application to geological problems. *Canadian Journal of Earth Sciences* **27**, 1431–50. <https://doi.org/10.1139/e90-152>
- Peressini G, Quick JE, Sinigoi S, Hofmann AW and Fanning M (2007) Duration of a large mafic intrusion and heat transfer in the lower crust: A SHRIMP U–Pb zircon study in the Ivrea–Verbano Zone (Western Alps, Italy). *Journal of Petrology* **48**, 1185–218.
- Petri B, Duretz T, Mohn G, Schmalholz SM, Karner GD and Müntener O (2019) Thinning mechanisms of heterogeneous continental lithosphere. *Earth and Planetary Science Letters* **512**, 147–62. <https://doi.org/10.1016/j.epsl.2019.02.007>
- Piazzolo S, Austrheim H and Whitehouse M (2012) Brittle-ductile microfabrics in naturally deformed zircon: Deformation mechanisms and consequences for U–Pb dating. *American Mineralogist* **97**, 1544–63.
- Putnis A, Janssen A, Jamtveit B and Putnis CV (2009) Reaction-induced fracturing during replacement reactions. *Geochimica et Cosmochimica Acta Supplement* **73**, A1061.
- Quick JE, Sinigoi S, Snoke AW, Kalakay TJ, Mayer A and Peressini G (2002) *Geologic Map of the Southern Ivrea–Verbano Zone, Northwestern Italy*. Reston, VA: U.S. Geological Survey. <https://doi.org/10.3133/i2776>
- Rapa G, Groppo C, Rolfo F, Petrelli M, Mosca P and Perugini D (2017) Titanite-bearing calc-silicate rocks constrain timing, duration and magnitude of metamorphic CO₂ degassing in the Himalayan belt. *Lithos* **292–293**, 364–78. <https://doi.org/10.1016/j.lithos.2017.09.024>
- Rasmussen B and Muhling JR (2007) Monazite begets monazite: Evidence for dissolution of detrital monazite and reprecipitation of syntectonic monazite during low-grade regional metamorphism. *Contributions to Mineralogy and Petrology* **154**, 675–89. <https://doi.org/10.1007/s00410-007-0216-6>
- Redler C, Johnson TE, White RW and Kunz BE (2012) Phase equilibrium constraints on a deep crustal metamorphic field gradient: Metapelitic rocks from the Ivrea Zone (NW Italy). *Journal of Metamorphic Geology* **30**, 235–54. <https://doi.org/10.1111/j.1525-1314.2011.00965.x>
- Regis D, Warren CJ, Mottram CM and Roberts NMW (2016) Using monazite and zircon petrochronology to constrain the P–T–t evolution of the middle crust in the Bhutan Himalaya. *Journal of Metamorphic Geology* **34**, 617–39. <https://doi.org/10.1111/jmg.12196>
- Rubatto D, Hermann J and Buick IS (2006) Temperature and bulk composition control on the growth of monazite and zircon during low-pressure anatexis (Mount Stafford, Central Australia). *Journal of Petrology* **47**, 1973–96. <https://doi.org/10.1093/petrology/egl033>
- Rutter E, Brodie K, James T and Burlini L (2007) Large-scale folding in the upper part of the Ivrea–Verbano zone, NW Italy. *Journal of Structural Geology* **29**, 1–17. <https://doi.org/10.1016/j.jsg.2006.08.013>
- Schmid R and Wood BJ (1976) Phase relationships in granulitic metapelites from the Ivrea–Verbano zone (Northern Italy). *Contributions to Mineralogy and Petrology* **54**, 255–79. <https://doi.org/10.1007/BF00389407>
- Schmid SM (1993) Ivrea Zone and adjacent Southern Alpine basement. In *Pre-Mesozoic Geology in the Alps* (eds JF von Raumer and F Neubauer), pp. 567–83. Berlin, Heidelberg: Springer. https://doi.org/10.1007/978-3-642-84640-3_33
- Schulz B (2021) Petrochronology of monazite-bearing garnet micaschists as a tool to decipher the metamorphic evolution of the Alpine basement. *Minerals* **11**, 981. <https://doi.org/10.3390/min11090981>
- Schuster R and Stüwe K (2008) Permian metamorphic event in the Alps. *Geology* **36**, 603–6.
- Scibiorski E, Kirkland CL, Kemp AIS, Tohver E and Evans NJ (2019) Trace elements in titanite: A potential tool to constrain polygenetic growth

- processes and timing. *Chemical Geology* **509**, 1–19. <https://doi.org/10.1016/j.chemgeo.2019.01.006>
- Seydoux-Guillaume A-M, Goncalves P, Wirth R and Deutsch A (2003) Transmission electron microscope study of polyphase and discordant monazites: Site-specific specimen preparation using the focused ion beam technique. *Geology* **31**, 973. <https://doi.org/10.1130/G19582.1>
- Seydoux-Guillaume AM, Paquette JL, Wiedenbeck M, Montel JM and Heinrich W (2002) Experimental resetting of the U–Th–Pb systems in monazite. *Chemical Geology* **191**, 165–81. [https://doi.org/10.1016/S0009-2541\(02\)00155-9](https://doi.org/10.1016/S0009-2541(02)00155-9)
- Shaw CA, Karlstrom KE, Williams ML, Jercinovic MJ and McCoy AM (2001) Electron-microprobe monazite dating of ca. 1.71–1.63 Ga and ca. 1.45–1.38 Ga deformation in the Homestake shear zone, Colorado: Origin and early evolution of a persistent intracontinental tectonic zone. *Geology* **29**, 739. [https://doi.org/10.1130/0091-7613\(2001\)029<0739:EMDOC>2.0.CO;2](https://doi.org/10.1130/0091-7613(2001)029<0739:EMDOC>2.0.CO;2)
- Siegesmund S, Layer P, Dunkl I, Vollbrecht A, Steenken A, Wemmer K and Ahrendt H (2008) Exhumation and deformation history of the lower crustal section of the Valstrona di Omegna in the Ivrea Zone, southern Alps. *Geological Society, London, Special Publications* **298**, 45–68. <https://doi.org/10.1144/SP298.3>
- Simonetti M, Carosi R, Montomoli C, Cottle JM and Law RD (2020) Transpressive deformation in the Southern European Variscan Belt: New insights from the Aiguilles Rouges Massif (Western Alps). *Tectonics* **39**. <https://doi.org/10.1029/2020TC006153>
- Simonetti M, Carosi R, Montomoli C, Law RD and Cottle JM (2021b) Unravelling the development of regional-scale shear zones by a multidisciplinary approach: The case study of the Ferrière-Mollières Shear Zone (Argentera Massif, Western Alps) *Journal of Structural Geology* **149**, 104399. <https://doi.org/10.1016/j.jsg.2021.104399>
- Simonetti M, Langone A, Bonazzi M, Corvò S and Maino M (2023) Tectono-metamorphic evolution of a post-variscan mid-crustal shear zone in relation to the Tethyan rifting (Ivrea-Verbano Zone, Southern Alps). *Journal of Structural Geology* **173**, 104896. <https://doi.org/10.1016/j.jsg.2023.104896>
- Simonetti M, Langone A, Corvò S and Bonazzi M (2021a) Triassic-Jurassic rift-related deformation and temperature-time evolution of the fossil Adriatic margin: A review from Ossola and Strona di Omegna valleys (Ivrea-Verbano Zone). *Ophioliti* **46**, 151–65. <https://doi.org/10.4454/ofioliti.v46i2.544>
- Sinigoï S, Quick JE, Mayer A and Budahn J (1996) Influence of stretching and density contrasts on the chemical evolution of continental magmas: An example from the Ivrea-Verbano Zone. *Contributions to Mineralogy and Petrology* **123**, 238–50. <https://doi.org/10.1007/s004100050153>
- Skrzypek E, Kato T, Kawakami T, Sakata S, Hattori K, Hirata T and Ikeda T (2018) Monazite behaviour and time-scale of metamorphic processes along a low-pressure/high-temperature field gradient (Ryoke Belt, SW Japan). *Journal of Petrology* **59**, 1109–44.
- Spandler C, Hammerli J, Sha P, Hilbert-Wolf H, Hu Y, Roberts E and Schmitz M (2016) MKED1: A new titanite standard for in situ analysis of Sm–Nd isotopes and U–Pb geochronology. *Chemical Geology* **425**, 110–26.
- Spear FS and Pyle JM (2010) Theoretical modeling of monazite growth in a low-Ca metapelite. *Chemical Geology* **273**, 111–9. <https://doi.org/10.1016/j.chemgeo.2010.02.016>
- Stacey JS and Kramers JD (1975) Approximation of terrestrial lead isotope evolution by a two-stage model. *Earth and Planetary Science Letters* **26**, 207–21.
- Stearns MA, Hacker BR, Ratschbacher L, Rutte D and Kylander-Clark ARC (2015) Titanite petrochronology of the Pamir gneiss domes: Implications for middle to deep crust exhumation and titanite closure to Pb and Zr diffusion. *Tectonics* **34**, 784–802. <https://doi.org/10.1002/2014TC003774>
- Taylor RJM, Clark C, Fitzsimons ICW, Santosh M, Hand M, Evans N and McDonald B (2014) Post-peak, fluid-mediated modification of granulite facies zircon and monazite in the Trivandrum Block, southern India. *Contributions to Mineralogy and Petrology* **168**, 1044. <https://doi.org/10.1007/s00410-014-1044-0>
- Terry MP, Robinson P, Hamilton MA and Jercinovic MJ (2000) Monazite geochronology of UHP and HP metamorphism, deformation, and exhumation, Nordøyane, Western Gneiss Region, Norway. *American Mineralogist* **85**, 1651–64. <https://doi.org/10.2138/am-2000-11-1208>
- Timms NE, Pearce MA, Erickson TM, Cavosie AJ, Rae AS, Wheeler J, Wittmann A, Ferrière L, Poelchau MH, Tomioka N, Collins GS, Gulick PS, Rasmussen C and Morgan JV (2019) New shock microstructures in titanite (CaTi–SiO₅) from the peak ring of the Chicxulub impact structure, Mexico. *Contributions to Mineralogy and Petrology* **174**, 1–23.
- Van Achterbergh E, Ryan C, Jackson S and Griffin W (2001) Appendix 3, Data reduction software for LA-ICP-MS. In *Laser-Ablation- ICPMS in the Earth Sciences* (ed P Sylvester), pp. 239–43. Ottawa, ON: Mineralogical Association of Canada. Short Course Series 29.
- Varga J, Raimondo T, Daczko NR and Adam J (2020) Experimental alteration of monazite in granitic melt: Variable U–Th–Pb and REE mobility during melt-mediated coupled dissolution-precipitation. *Chemical Geology* **544**, 119602. <https://doi.org/10.1016/j.chemgeo.2020.119602>
- Vavra G, Schmid R and Gebauer D (1999) Internal morphology, habit and U–Th–Pb microanalysis of amphibolite-to-granulite facies zircons: Geochronology of the Ivrea Zone (Southern Alps). *Contributions to Mineralogy and Petrology* **134**, 380–404. <https://doi.org/10.1007/s004100050492>
- Vermeesch P (2018) IsoplotR: A free and open toolbox for geochronology. *Geoscience Frontiers* **9**, 1479–93. <https://doi.org/10.1016/j.gsf.2018.04.001>
- Walters JB, Cruz-Urbe AM, Song WJ, Gerbi C and Biela K (2022) Strengths and limitations of in situ U–Pb titanite petrochronology in polymetamorphic rocks: An example from western Maine, USA. *Journal of Metamorphic Geology* **40**, 1043–66. <https://doi.org/10.1111/jmg.12657>
- Wawrzynitz N, Krohe A, Rhede D and Romer RL (2012) Dating rock deformation with monazite: The impact of dissolution precipitation creep. *Lithos* **134–135**, 52–74. <https://doi.org/10.1016/j.lithos.2011.11.025>
- Weinberg RF, Wolfram LC, Nebel O, Hasalová P, Závada P, Kylander-Clark ARC and Becchio R (2020) Decoupled U–Pb date and chemical zonation of monazite in migmatites: The case for disturbance of isotopic systematics by coupled dissolution-reprecipitation. *Geochimica et Cosmochimica Acta* **269**, 398–412. <https://doi.org/10.1016/j.gca.2019.10.024>
- Wheeler J, Mariani E, Piazzolo S, Prior DJ, Trimby P and Drury MR (2009) The weighted Burgers vector: A new quantity for constraining dislocation densities and types using Electron Backscatter Diffraction on 2D sections through crystalline materials. *Journal of Microscopy* **233**, 482–94.
- Wheeler J, Piazzolo S, Prior DJ, Trimby P and Tielke JA (2024) Using crystal-lattice distortion data for geological investigations: The weighted Burgers vector method. *Journal of Structural Geology* **179**, 105040.
- Whitney DL and Evans BW (2010) Abbreviations for names of rock-forming minerals. *American Mineralogist* **95**, 185–7.
- Williams MA, Kelsey DE, Baggs T, Hand M and Alessio KL (2018) Thorium distribution in the crust: Outcrop and grain-scale perspectives. *Lithos* **320**, 222–35.
- Williams MA, Kelsey DE and Rubatto D (2022) Thorium zoning in monazite: A case study from the Ivrea–Verbano zone, NW Italy. *Journal of Metamorphic Geology* **40**, 1015–42. <https://doi.org/10.1111/jmg.12656>
- Williams ML and Jercinovic MJ (2002) Microprobe monazite geochronology: Putting absolute time into microstructural analysis. *Journal of Structural Geology* **24**, 1013–28. [https://doi.org/10.1016/S0191-8141\(01\)00088-8](https://doi.org/10.1016/S0191-8141(01)00088-8)
- Williams ML and Jercinovic MJ (2012) Tectonic interpretation of metamorphic tectonites: Integrating compositional mapping, microstructural analysis and in situ monazite dating. *Journal of Metamorphic Geology* **30**, 739–52. <https://doi.org/10.1111/j.1525-1314.2012.00995.x>
- Wolff R, Dunkl I, Kiesselbach G, Wemmer K and Siegesmund S (2012) Thermochronological constraints on the multiphase exhumation history of the Ivrea-Verbano Zone of the Southern Alps. *Tectonophysics* **579**, 104–17. <https://doi.org/10.1016/j.tecto.2012.03.019>
- Wyatt DC, Smye AJ, Garber JM and Hacker BR (2022) Assembly and tectonic evolution of continental lower crust: Monazite petrochronology of the Ivrea-Verbano Zone (Val Strona di Omegna). *Tectonics* **41**. <https://doi.org/10.1029/2021TC006841>
- Xypolias P (2010) Vorticity analysis in shear zones: A review of methods and applications. *Journal of structural Geology* **32**, 2072–92.
- Zingg A (1990) The Ivrea Crustal Cross-Section (Northern Italy and Southern Switzerland). In *Exposed Cross-Sections of the Continental Crust* (eds MH Salisbury and DM Fountain), pp. 1–19. Netherlands: Springer. https://doi.org/10.1007/978-94-009-0675-4_1